empty

Topics in Tau Neutrino Astronomy

Student: **Fei-Fan Lee** Advisor: **Guey-Lin Lin**

Department of Physics

National Chiao-Tung University

Abstract

Neutrino astronomy is currently a subject of great interest, promising to expand our observational range of the Universe. Therefore, in this thesis, we discuss some interesting topics in tau neutrino astronomy. In the first part of this thesis, we present a semi-analytic calculation of the tau-lepton flux emerging from the Earth induced by incident high energy neutrinos interacting inside the Earth for $10^5 \leq E_\nu/\text{GeV} \leq 10^{10}$. We obtain results for the energy dependence of the tau-lepton flux coming from the Earth-skimming neutrinos, because of the neutrino-nucleon charged-current scattering as well as the resonant$\bar{\nu}_e e^-$ scattering. We illustrate our results for several anticipated high energy astrophysical neutrino sources such as the active galactic nuclei, the gamma-ray bursts, and the Greisen-Zatsepin-Kuzmin neutrino fluxes. In the second part of this thesis, we point out the opportunity of the tau neutrino astronomy for neutrino energies of the order 1 to 10^4 GeV's. In this energy range, it is demonstrated that the flavor dependence in the background atmospheric neutrino flux leads to the drastically different prospects between the observation of astrophysical muon neutrinos and that of astrophysical tau neutrinos. Taking the galactic-plane neutrino flux as the targeted astrophysical source, we found that the galactic-plane tau neutrino flux dominates over the atmospheric tau neutrino flux for $E \geq 10$ GeV. Hence, the galactic-plane can in principle be seen through tau neutrinos with energies greater than 10 GeV, but the galactic-plane muon neutrino flux is overwhelmed by its atmospheric background until $E \geq 10^6$ GeV.

empty

Contents

List of Tables

List of Figures

Chapter 1

Introduction

Neutrino astronomy is currently a subject of great interest, promising to expand our observational range of the Universe. The high-energy neutrinos ($E_\nu > 10^3$ GeV) may carry information from the sources of the highest energy phenomena ever observed in cosmic rays, possibly coming from active galactic nuclei (AGN) or gamma ray bursts (GRB). They may probe the early stages of the Universe at its farthest distances. In addition, they will contribute to the search of weakly interacting massive particles (WIMP), supernova explosions, monopoles, besides the discovery potential for new physics. Therefore, detecting high energy neutrinos is important to identify the extreme energy sources in the Universe, and possibly to unveil the puzzle of cosmic rays with energy above the GZK cutoff [1].

There are two different strategies to detect the footprints of high energy neutrinos. The first strategy is implemented by installing detectors in a large volume of ice or water where most of the scatterings between the candidate neutrinos and nucleons occur essentially inside the detector, whereas the second strategy aims at detecting the air showers caused by the charged leptons produced by the neutrino-nucleon scatterings taking place inside the Earth or in the air, far away from the instrumented volume of the detector. The latter strategy thus include the possibility of detection of quasi horizontal incident

neutrinos which are also referred to as the Earth-skimming neutrinos. These neutrinos are considered to interact below the horizon of an Earth based surface detector.

The second strategy has been proposed in 2002 [2]. The Pierre Auger observatory group has simulated the anticipated detection of the air-showers from the decays of τ leptons [3]. The tau air-shower event rates resulting from the Earth-skimming tau neutrinos for different high energy neutrino telescopes are given in [4]. A Monte-Carlo study of tau air-shower event rate was also reported [5]. We note that Ref. [4] does not consider the tau-lepton energy distribution in the ν_τ-nucleon scattering, and only the incident tau neutrinos with energies greater than 10^8 GeV are considered. For Ref. [5], we note that only the sum of tau air-shower event rates arising from different directions is given. Hence some of the events may be due to tau-leptons/neutrinos traversing a large distance. As a result, it is not possible to identify the source of tau-neutrino flux even with the observation of tau-lepton induced air-shower. In Chap. 2, we will concentrate on the high energy Earth-skimming neutrinos for $10^5 \leq E_\nu/\text{GeV} \leq 10^{10}$ and shall calculate the energy spectrum of their induced tau-leptons, taking into account the `inelasticity` of neutrino-nucleon scatterings and the tau-lepton `energy loss` in detail [6]. Our work differs from Ref. [5] by our emphasis on the Earth-skimming neutrinos. We shall present our results in the form of outgoing tau-lepton spectra for different distances inside the rock, instead of integrating the energy spectra. As will be demonstrated, such spectra are insensitive to the distances traversed by the Earth-skimming ν_τ and τ. They are essentially determined by the tau lepton range. Because of this characteristic feature, our results are useful for setting up simulations with specifically chosen air-shower content detection strategy, such as detection of the Cherenkov radiation or the air fluorescence. Our results are also useful for the coherent Cherenkov radio emission measurement detectors such as the Radio Ice Cherenkov Experiment (RICE) [7] and the Antarctic Impulsive Transient Array (ANITA) [8].

Besides studying high energy tau neutrinos, this thesis also point out the opportunity of tau neutrino astronomy for neutrino energies of the order 10 GeV to 10^3 GeV [9]. It is understood that the importance of observing ν_τ is twofold. First, seeing the ν_τ confirms the atmospheric $\nu_\mu \to \nu_\tau$ oscillation scenario which is so far established only by the ν_μ disappearance measurement [32]. Second, since the atmospheric ν_τ flux is generally suppressed as compared to the atmospheric ν_μ flux, the prospective observation of the astrophysical ν_τ suffers `much less` background than in the ν_μ case. In Chap. 3, we shall address the second point. In the GeV to TeV energy range, the intrinsic tau neutrino production is suppressed relative to the intrinsic muon neutrino production. Any sizable tau neutrino flux must arise due to the $\nu_\mu \to \nu_\tau$ neutrino oscillations only. It is demonstrated that, in the presence of the neutrino oscillations, consideration of the neutrino flavor dependence in the background atmospheric neutrino flux leads to the drastically different prospects between the observation of the astrophysical tau neutrinos and that of the astrophysical muon neutrinos. Taking the galactic-plane neutrino flux as the targeted astrophysical source, we have found that the galactic-plane tau neutrino flux dominates over the atmospheric tau neutrino flux for $E \geq 10$ GeV. Hence, the galactic-plane can in principle be seen through the tau neutrinos with energies just greater than 10 GeV. In a sharp contrast, the galactic-plane muon neutrino flux is overwhelmed by its atmospheric background until the energy of 10^6 GeV.

We present our conclusion in Chap. 4, while some technical details are discussed in Appendix A.

Chapter 2

Earth-Skimming Tau Neutrinos and the Induced Tau-Lepton Spectrum

2.1 Tau-Lepton Energy Spectrum

The evolution of various fluxes in the medium is governed by the transport equations. Taking into account only the neutrino-nucleon scatterings, the transport equations for tau neutrinos and tau leptons are

$$\frac{\partial F_{\nu_\tau}(E,X)}{\partial X} = -\frac{F_{\nu_\tau}(E,X)}{\lambda_{\nu_\tau}(E)} + n_N \sum_{i=1}^{3} \int_{y^i_{\min}}^{y^i_{\max}} \frac{\mathrm{d}y}{1-y} F_i(E_y, X) \frac{\mathrm{d}\sigma^i_\nu}{\mathrm{d}y}(y, E_y), \quad (2.1)$$

and

$$\begin{aligned} \frac{\partial F_\tau(E,X)}{\partial X} &= -\frac{F_\tau(E,X)}{\lambda^{\mathrm{cc}}_\tau(E)} - \frac{F_\tau(E,X)}{\rho d_\tau(E)} + \frac{\partial\left[(\alpha(E)+\beta(E)E)F_\tau(E,X)\right]}{\partial E} \\ &+ n_N \int_{y_{\min}}^{y_{\max}} \frac{\mathrm{d}y}{1-y} F_{\nu_\tau}(E_y, X) \frac{\mathrm{d}\sigma_{\nu_\tau N\to\tau Y}}{\mathrm{d}y}(y, E_y), \end{aligned} \quad (2.2)$$

where n_N the number of target nucleons per unit medium mass, and ρ is the mass density of the medium. The $\sigma^{1,2,3}_\nu$ are defined as $\sigma(\nu_\tau + N \to \nu_\tau + Y)$, $\Gamma(\tau \to \nu_\tau + Y)/c\rho n_N$, and $\sigma(\tau + N \to \nu_\tau + Y)$ respectively. The quantity X represents the slant depth traversed by the particles, i.e., the amount of medium per unit area traversed by the particle (and thus in units of g/cm^2). The λ_ν,

d_τ, and $\lambda_\tau^{\rm CC}$ represent the ν_τ interaction thickness, the tau-lepton decay length, and the tau-lepton charged-current interaction thickness respectively, with, say, $\lambda_\nu^{-1} = n_N \sigma_{\nu N}$ and $d_\tau = c\tau_\tau E/m_\tau$. The E_y is equal to $E/(1-y)$, where y is the inelasticity of neutrino-nucleon scatterings, such that the initial and final-state particle energies in the differential cross sections ${\rm d}\sigma_\nu^i(y, E_y)/{\rm d}y$ and ${\rm d}\sigma_{\nu_\tau N\to\tau Y}(y, E_y)/{\rm d}y$ are $E/(1-y)$ and E respectively. The limits for y, $y^i_{\rm min}$ and $y^i_{\rm max}$ depend on the kinematics of each process. Finally, the energy-loss coefficients $\alpha(E)$ and $\beta(E)$ are defined by $-{\rm d}E/{\rm d}X = \alpha(E) + \beta(E)E$ with E the energy being the tau lepton. An equation similar to Eq. (2.2) in the context of atmospheric muons was found in Ref. [10].

It is important to know the energy-loss coefficients $\alpha(E)$ and $\beta(E)$. As mentioned before [11], the coefficient $\alpha(E)$ is due to the energy loss by the ionization [49], while $\beta(E)$ is contributed by the bremsstrahlung [13], the e^+e^- pair production [14] and the photo-nuclear processes [11, 15]. It is understood that the contribution by $\alpha(E)$ becomes unimportant for $E \geq 10^5$ GeV. The coefficient $\beta(E)$ can be parameterized as $\beta(E) = (1.6 + 6(E/10^9{\rm GeV})^{0.2}) \times 10^{-7}{\rm g}^{-1}{\rm cm}^2$ in the standard rock for $10^5 \leq E/{\rm GeV} \leq 10^{12}$.

Before calculating the tau-lepton flux, we want to check the tau-lepton range given by our semi-analytic approach. To do this, we rewrite Eq. (2.2) by dropping the neutrino term, i.e.,

$$\frac{\partial F_\tau(E,X)}{\partial X} = -\frac{F_\tau(E,X)}{\lambda_\tau^{\rm cc}(E)} - \frac{F_\tau(E,X)}{\rho d_\tau(E)} + \frac{\partial\left[\gamma(E)F_\tau(E,X)\right]}{\partial E}, \tag{2.3}$$

with $\gamma(E) \equiv \alpha(E) + \beta(E)E$. One can easily solve it for $F_\tau(E,X)$:

$$F_\tau(E,X) = F_\tau(\bar{E},0)\exp\left[\int_0^X {\rm d}T\left(\gamma'(\bar{E}) - \frac{1}{\rho d_\tau(\bar{E})} - \frac{1}{\lambda_\tau^{\rm cc}(\bar{E})}\right)\right], \tag{2.4}$$

where $\bar{E} \equiv \bar{E}(X;E)$ with ${\rm d}\bar{E}/{\rm d}X = \gamma(\bar{E})$ and $\bar{E}(0;E) = E$. To calculate the tau-lepton range, we substitute $F_\tau(E,0) = \delta(E - E_0)$. The survival probability $P(E_0,X)$ for a tau-lepton with an initial energy E_0 at $X = 0$ is

$$P(E_0,X) = \frac{\gamma(\tilde{E}_0)}{\gamma(E_0)}\exp\left[\int_0^X {\rm d}T\left(\gamma'(\tilde{E}_0) - \frac{1}{\rho d_\tau(\tilde{E}_0)} - \frac{1}{\lambda_\tau^{\rm cc}(\tilde{E}_0)}\right)\right], \tag{2.5}$$

where $\tilde{E}_0 \equiv \tilde{E}(X; E_0)$ with $\mathrm{d}\tilde{E}_0/\mathrm{d}X = -\gamma(\tilde{E}_0)$ and $\tilde{E}_0(0; E_0) = E_0$. The tau-lepton range is simply

$$R_\tau(E_0) = \int_0^\infty \mathrm{d}X P(E_0, X). \tag{2.6}$$

For $E_0 = 10^9$ GeV, we find that $R_\tau = 10.8$ km in the standard rock ($Z = 11$, $A = 22$) while $R_\tau = 5.0$ km in the iron. Both values are in good agreement with those obtained by Monte-Carlo calculations [11]. To compare the tau-lepton ranges, we have followed the convention in Ref. [11] by requiring the final tau-lepton energy $\tilde{E}(X; E_0)$ to be greater than 50 GeV.

It is noteworthy that we obtain R_τ by using the `continuous` tau-lepton energy-loss approach, rather than stochastic approach adopted in Ref. [11]. In the muon case, the continuous approach to the muon energy loss is known to overestimate the muon range [16]. Such an overestimate is not significant in the tau-lepton case, because of the decay term in Eq. (2.5). In fact, tau lepton decay term dictates the tau range in the rock until $E_\tau \geq 10^7$ GeV. Even for $E_\tau > 10^7$ GeV, the tau lepton range is still not entirely determined by the tau-lepton energy loss. Hence different treatments on the tau-lepton energy loss do not lead to large differences in the tau-lepton range, in contrast to the case for the muon range. Our result for the tau-lepton range up to 10^{12} GeV are plotted in Fig. 2.1. This is an extension of the result in Ref. [11], where the tau-lepton range is calculated only up to 10^9 GeV. Our extension is seen explicitly in the addition of charged-current scattering term on the R.H.S. of Eq. (2.3). This term is necessary because $1/\lambda_\tau^{\mathrm{CC}}$ becomes comparable to $1/\rho d_\tau$ in the rock for $E \geq 10^{10}$ GeV; whereas one does not need to include the contribution by the tau-lepton neutral-current scattering, since such a contribution can not compete with the last term in Eq. (2.3) until $E \geq 10^{16}$ GeV [11]. We remark that our extended results for R_τ are subject to the uncertainties of neutrino-nucleon scattering cross section at high energies. We use the CTEQ6 parton distribution functions [17] in this work, and at the high energy (the small x region, namely for $x < 10^{-6}$), we fit these parton distribution functions into the

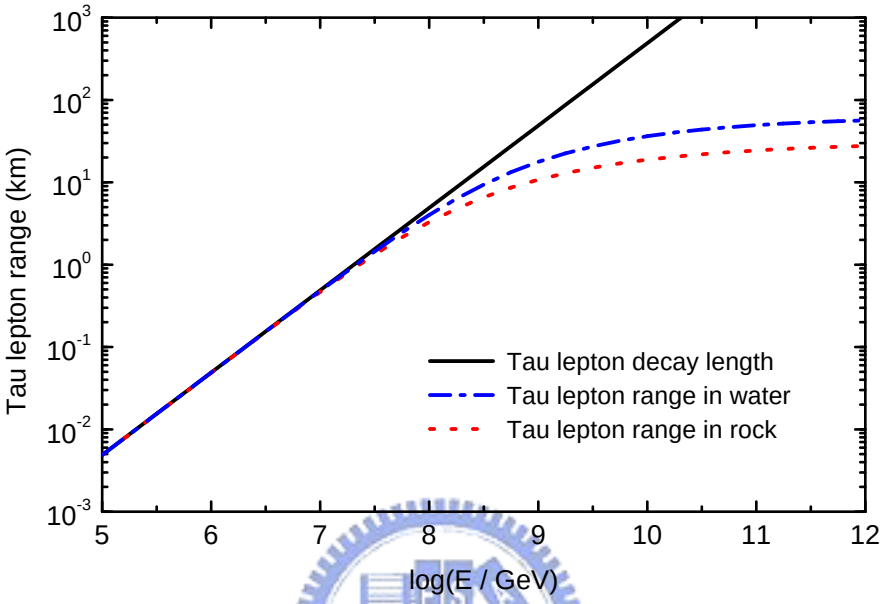

Figure 2.1: The tau-lepton range in rock and in water using Eq. [3.1] and the tau-lepton decay length d_τ in km as a function of tau-lepton energy in GeV.

form proportional to $x^{-1.3}$ as a guide.

Having checked the tau-lepton range, we now turn to the case of tau-lepton production by the $\nu_\tau - N$ charged-current scattering. Once the incoming ν_τ flux is given, the tau-lepton flux can be solved from Eqs. (2.1) and (2.2). The ν_τ flux can be calculated by the following ansatz [18]:

$$F_{\nu_\tau}(E, X) = F_{\nu_\tau}(E, 0) \exp\left(-\frac{X}{\Lambda_\nu(E, X)}\right), \tag{2.7}$$

where $\Lambda_\nu(E, X) = \lambda_\nu(E)/\left(1 - Z_\nu(E, X)\right)$, with the factor $Z_\nu(E, X)$ arising from the regeneration effect of the ν_τ flux. On the other hand, the tau-lepton

flux is given by

$$F_\tau(E,X) = \int_0^X \mathrm{d}T G_\nu(\bar{E},T) \times \exp\left[\int_T^X \mathrm{d}T' \left(\gamma'(\bar{E}) - \frac{1}{\rho d_\tau(\bar{E})} - \frac{1}{\lambda_\tau^{\mathrm{cc}}(\bar{E})}\right)\right], \quad (2.8)$$

with $\bar{E} \equiv \bar{E}(X-T;E)$, $\gamma(E) \equiv \alpha(E) + \beta(E)E$, and

$$G_\nu(E,X) = n_N \int_{y_{\min}}^{y_{\max}} \frac{\mathrm{d}y}{1-y} F_\nu(E_y,X) \frac{\mathrm{d}\sigma_{\nu_\tau N\to\tau Y}}{\mathrm{d}y}(y,E_y). \quad (2.9)$$

We can see that the factor $Z_\nu(E,X)$ enters into the expression for $F_\tau(E,X)$ through the function $G_\nu(E,X)$. Similarly, $Z_\nu(E,X)$ also depends on $F_\tau(E,X)$. It is possible to solve for $Z_\nu(E,X)$ and $F_\tau(E,X)$ simultaneously by the iteration method [18]. The details are given in Appendix A.

2.2 W Resonance Contributions

Let us now discuss the case of tau-lepton production by the Glashow resonance [19, 20], namely, via $\bar{\nu}_e e^- \to W \to \bar{\nu}_\tau \tau^-$, also. For the Glashow resonance, it is well known that

$$\sigma(\bar{\nu}_e e^- \to W^- \to \bar{\nu}_\tau \tau^-) = \frac{G_F^2 m_W^4}{3\pi} \cdot \frac{s}{(s-m_W^2)^2 + m_W^2 \Gamma_W^2}, \quad (2.10)$$

with $s = 2m_e E_{\bar{\nu_e}}$ and $1/\sigma \cdot \mathrm{d}\sigma/\mathrm{d}z = 3(1-z)^2$, where $z = E_\tau/E_{\bar{\nu}_e}$.The transport equation for $\bar{\nu}_e$ and tau leptons are then given by

$$\frac{\partial F_{\bar{\nu}_e}(E,X)}{\partial X} = -\frac{F_{\bar{\nu}_e}(E,X)}{\lambda_{\bar{\nu}_e}(E)} + n_N \int_{y_{\min}}^{y_{\max}} \frac{\mathrm{d}y}{1-y} F_{\bar{\nu}_e}(E_y,X) \frac{\mathrm{d}\sigma_{\bar{\nu}_e N\to\bar{\nu}_e Y}}{\mathrm{d}y}(y,E_y), \quad (2.11)$$

and

$$\frac{\partial F_\tau(E,X)}{\partial X} = -\frac{F_\tau(E,X)}{\lambda_\tau^{\mathrm{cc}}(E)} - \frac{F_\tau(E,X)}{\rho d_\tau(E)} + n_e \int_{y_{\min}}^{y_{\max}} \frac{\mathrm{d}y}{1-y} F_{\bar{\nu}_e}(E_y,X) \frac{\mathrm{d}\sigma_{\bar{\nu}_e e^-\to\bar{\nu}_\tau\tau^-}}{\mathrm{d}y}(y,E_y), \quad (2.12)$$

where n_e is the number of target electrons per unit medium mass, and y is the inelasticity of $\bar{\nu}_e e^-$ resonant scattering.

For solving the above coupled transport equations, we shall focus our attention only on those $\bar{\nu}_e$'s for which $E_{\bar{\nu}_e}$ satisfies the resonance condition, i.e., $E_{\bar{\nu}_e} \approx E_R \equiv m_W^2/2m_e$. It is clear from Eq. (2.12) that $F_\tau(E,X)$ only depends on $F_{\bar{\nu}_e}(E_R,X)$, because of the narrow peak nature of $\bar{\nu}_e e^-$ scattering cross section. One also expects that $F_\tau(E,X)$ is only significant for E around the resonance energy E_R. In this energy region, one may neglect the first term on the R.H.S. of Eq. (2.12) in comparison with the second term.

We can simplify the last term in Eq. (2.12) by using

$$\frac{\mathrm{d}\sigma_{\bar{\nu}_e e^- \to \bar{\nu}_\tau \tau^-}}{\mathrm{d}z}(z, E/z) = \frac{m_W^4 G_F^2}{\pi} \frac{s(1-z)^2}{(s-m_W^2)^2 + m_W^2 \Gamma_W^2}, \tag{2.13}$$

with $z = 1 - y$, and the narrow-width approximation

$$\frac{1}{\pi} \frac{m_W \Gamma_W}{(s-m_W^2)^2 + m_W^2 \Gamma_W^2} \approx \delta(s - m_W^2). \tag{2.14}$$

Then arriving at

$$\frac{\partial F_\tau(E,X)}{\partial X} = -\frac{F_\tau(E,X)}{\rho d_\tau(E)} + \frac{1}{3}\left(1 - \frac{E}{E_R}\right)^2 \left(\frac{\pi \Gamma_W}{L_R m_W}\right) F_{\bar{\nu}_e}(E_R, X), \tag{2.15}$$

where $E_R = m_W^2/2m_e$ is the $\bar{\nu}_e$ energy such that the W boson is produced on-shell in the $\bar{\nu}_e e^-$ scattering. The $L_R \equiv 1/n_e \sigma_{\bar{\nu}_e e^- \to W^-}$ is the interaction thickness for such a scattering. To solve for $F_\tau(E,X)$, we need to input $F_{\bar{\nu}_e}(E_R,X)$. Obviously, the $\bar{\nu}_e$ flux at the resonant-scattering energy E_R is mainly attenuated by the resonant scattering itself. Hence $F_{\bar{\nu}_e}(E_R,X) = \exp(-X/L_R) F_{\bar{\nu}_e}(E_R,0)$. Substituting this result into Eq. (2.15), we obtain

$$\begin{aligned} F_\tau(E,X) &= \frac{1}{3}\left(1 - \frac{E}{E_R}\right)^2 \left(\frac{\pi \Gamma_W}{L_R m_W}\right) F_{\bar{\nu}_e}(E_R,0) \exp\left(-\frac{X}{\rho d_\tau(E)}\right) \\ &\times \int_0^X \mathrm{d}Z \exp\left[\left(\frac{1}{\rho d_\tau(E)} - \frac{1}{L_R}\right) Z\right]. \end{aligned} \tag{2.16}$$

The integration over Z can be easily performed. In practice, it is obvious that

$X \gg \rho d_\tau(E)$. In this limit, we have

$$F_\tau(E,X) = \frac{\pi}{3}\left(1-\frac{E}{E_R}\right)^2\left(\frac{\Gamma_W}{m_W}\right)\left(\frac{\rho d_\tau(E)}{L_R}\right)F_{\bar{\nu}_e}(E_R,0)\exp\left(-\frac{X}{L_R}\right). \quad (2.17)$$

Let us consider standard rock as the medium for $\bar{\nu}_e e^-$ scattering, we then have $\rho/L_R = n_e\rho\sigma_{\bar{\nu}_e e^-\to W^-}$. Given $\sigma_{\bar{\nu}_e e^-\to W^-} = 4.8\cdot 10^{-31}$ cm^2 at the W boson mass peak, and $n_e\rho = 2.65\times 6.0/2\times 10^{23}/\text{cm}^3$ in the standard rock, we obtain $\rho/L_R = (26\,\text{km})^{-1}$. Furthermore, we can write $d_\tau(E) = 49\,\text{km}\times(E/10^6\text{GeV})$. We then obtain the following ratio

$$\frac{F_\tau(E,X)}{F_{\bar{\nu}_e}(E_R,0)} = 3.3\cdot 10^{-4}\times\left(\frac{E}{E_R}\right)\times\left(1-\frac{E}{E_R}\right)^2\times\exp\left(-\frac{X}{L_R}\right). \quad (2.18)$$

In water, the prefactor $3.3\cdot 10^{-4}$ becomes $1.4\cdot 10^{-4}$. It is to be noted that $E < E_R$ in the above equation. We will see later that the contribution to $F_\tau(E,X)$ by the W-resonance is negligible compared to that by the $\nu_\tau - N$ scattering.

2.3 The Results

In this section, we will present the tau-lepton energy spectrum induced by three kinds of diffuse astrophysical neutrino fluxes: the AGN [21], GRB [22] and GZK [23] neutrino fluxes. These three models show that: The $p\gamma$ interactions in cosmos will produce the intrinsic F_{ν_μ}, and then $F_{\nu_\tau} = 1/2\cdot F_{\nu_\mu}$ because of (two) neutrino flavor oscillations during propagation [24]. Our convention for F_{ν_τ} is that $F_{\nu_\tau} = \text{d}N_{\nu_\tau}/\text{d}(\log_{10}E)$ in the unit of cm^{-2} s^{-1} sr^{-1}. The same convention is used for the outgoing tau lepton fluxes. For completeness, let us remark here that the upper bound on diffuse astrophysical F_{ν_μ} (not F_{ν_τ}) from the Antarctic Muon and Neutrino Detector Array (AMANDA) B10 is of the order of $\sim 8.4\times 10^{-7}$ cm^{-2} s^{-1} sr^{-1} GeV for $6\times 10^3 \le E_\nu/\text{GeV} \le 10^6$ [25]. This 90% classical confidence upper bound is mainly for upward going ν_μ with E^{-2} energy spectrum and includes the systematic uncertainties. As far as the AMANDA B10 upper bound on F_{ν_μ} is concerned, all three of our representative

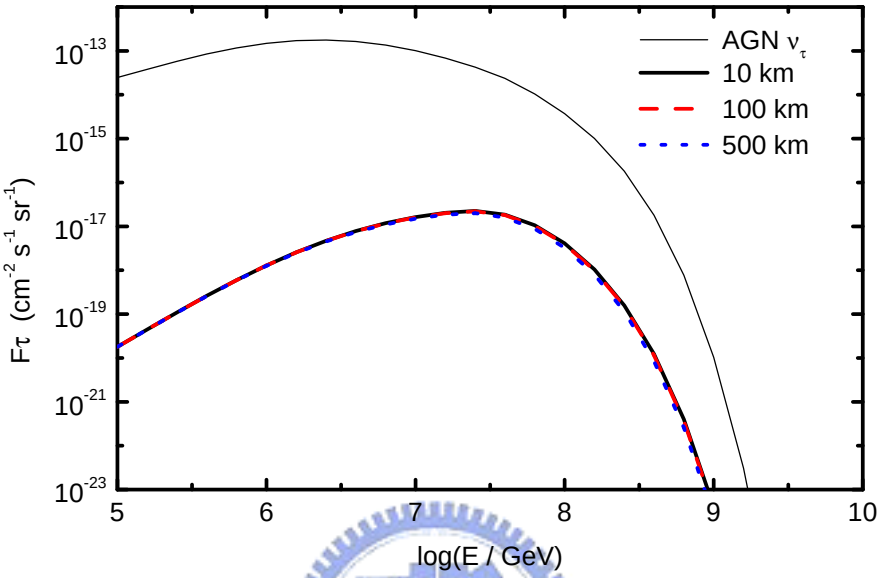

Figure 2.2: The tau-lepton energy spectrum induced by the AGN neutrinos in rock for three different X/ρ ratio values (see text for more details). The incident tau-neutrino flux is shown by the thin solid line.

neutrino flux models are clearly compatible with this upper bound within its energy range.

Incorporating all the formulae above, we show in Fig. 2.2 the outgoing tau-lepton energy spectra resulting from the propagation of incident AGN neutrinos inside the rock ($\rho = 2.65$ g/cm^3) for $X/\rho = 10$ km, 100 km and 500 km respectively. The noteworthy point is the fact that the tau-lepton energy spectra remain almost unchanged for the above three different slant depths/matter density ratio values. We can understand this feature by two simple facts. First, the neutrino-nucleon charged-current interaction length, which is related to the interaction thickness by $\lambda_{\rm CC} = \rho l_{\rm CC}$, is given by $l_{\rm CC} = 2 \cdot 10^4$ km $[(1\ {\rm g/cm}^3/\rho)]$ $[E_\nu/(10^6\ {\rm GeV})]^{-0.363}$. Secondly, the tau leptons, which eventually exit the

Earth, ought to be produced within a tau-lepton-range distance to the exit point. For a tau-lepton produced far away from the exit point, it loses energy and decays before reaching to the exit point. Hence the tau-lepton flux is primarily determined by the ratio of tau-lepton range to the charged current neutrino-nucleon interaction length. The total slant depth X which the tau-neutrino (tau-lepton) traverses inside the Earth is then unimportant, unless X is large enough such that the tau neutrino flux attenuates significantly before tau-neutrino is converted into the tau-lepton. We note that the typical energy for the AGN neutrinos, in which this flux peaks, is between 10^5 and 10^8 GeV. The corresponding neutrino-nucleon neutral current interaction length then ranges from $42,000$ km down to $3,400$ km, given $l_{\rm NC} = 2.35 \cdot l_{\rm CC}$. Hence, even for X/ρ as large as 500 km, the attenuation of the tau neutrino flux is negligible. This explains the insensitivity of tau-lepton flux with respect to our chosen X/ρ values for the AGN case. The situation is rather similar for the tau-lepton flux resulting from the GRB tau neutrinos (see Fig. 2.3). On the other hand, a slight suppression is found for the GZK case at $E_\tau > 10^9$ GeV as one increases X/ρ from 10 km to 500 km (see Fig. 2.4). This is because the typical GZK tau neutrino flux peaks for energy range between 10^7 and 10^{10} GeV, which corresponds to attenuation lengths ranging from $7,800$ km down to 640 km. One notices that 640 km is rather close to the distance 500 km which we choose for X/ρ. Hence a slight suppression on the tau-lepton flux occurs for $X/\rho = 500$ km.

After comparing our AGN-type tau-lepton flux with that obtained by Monte-Carlo simulations which are adopting stochastic approach for the tau-lepton energy loss [26], we find that these two tau-lepton fluxes agree within $\sim 10\%$. This result is expected since the tau-lepton range obtained by the above two approaches agree well, as mentioned before. It is easily seen from Figs. 2.2 - 2.4 that the AGN case has a largest tau-lepton flux between 10^6 and 10^8 GeV. Because the resonant $\bar{\nu}_e - e^-$ scattering cross section peaks at $E_\nu = 6.3 \cdot 10^6$ GeV,

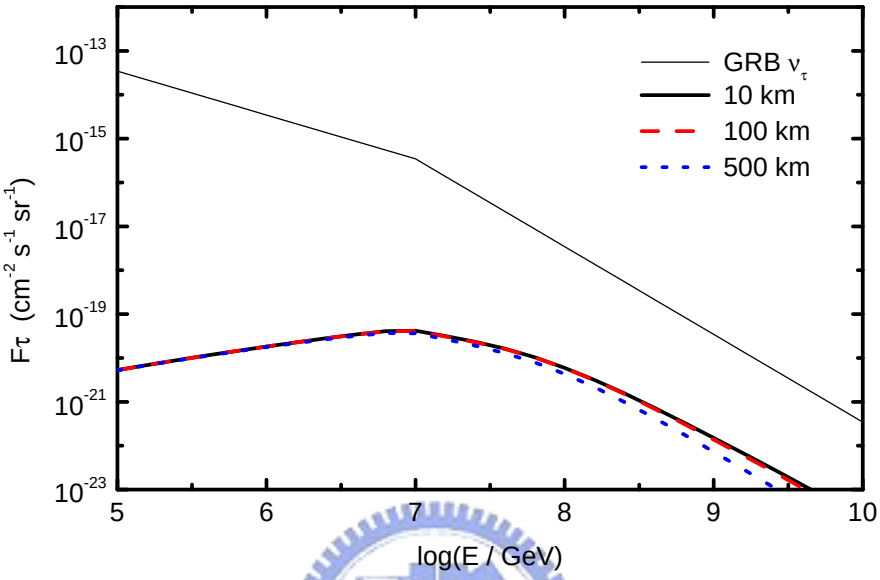

Figure 2.3: The tau-lepton energy spectrum induced by the GRB neutrinos in rock for three different X/ρ ratio values (see text for more details). The incident tau-neutrino flux is shown by the thin solid line.

it is interesting to compare the integrated tau-lepton flux arising from this scattering to the one resulting from neutrino-nucleon scattering. For the resonant $\bar{\nu}_e - e^-$ scattering, we integrate the tau-lepton energy spectrum from 10^6 GeV to $6.3 \cdot 10^6$ GeV, and obtain $\Phi_\nu^{\rm R} = 0.08$ km^{-2}sr^{-1}yr^{-1}. For neutrino-nucleon scattering, we find that $\Phi_\nu^{\rm CC} = 2.2$ km^{-2}sr^{-1}yr^{-1} by integrating the corresponding tau-lepton energy spectrum from 10^6 GeV to 10^7 GeV. The detailed results for $\Phi_\nu^{\rm CC}$ are summarized in Table 2.1. The entries in the Table entitled *full* are obtained using the F_τ obtained in this work, whereas the approximated values entitled *approx* are obtained by following the description given in Ref. [4], which uses a constant β and a constant inelasticity coefficient for $\nu_\tau N$ scattering. We remark that the authors in Ref. [4] have taken E to be greater than 10^8 GeV.

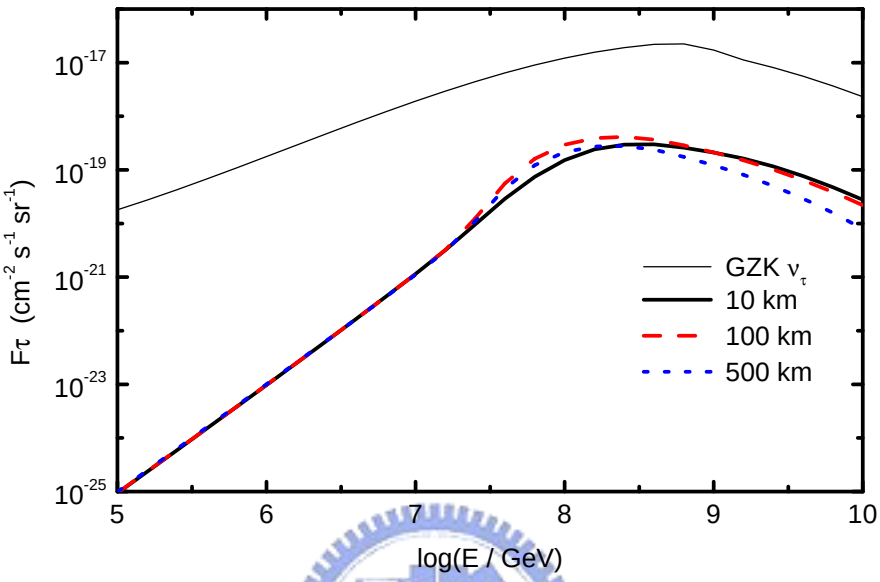

Figure 2.4: The tau-lepton energy spectrum induced by the GZK neutrinos in rock for three different X/ρ ratio values (see text for more details). The incident tau-neutrino flux is shown by the thin solid line.

Hence the integrated fluxes in the column *approx* with energies less than 10^8 GeV are taken as extrapolations. Thus, one should compare the two integrated fluxes only for $E > 10^8$ GeV. It is easily seen that the two integrated fluxes seem to agree for $E > 10^8$ GeV. Besides the integrated fluxes for $E > 10^8$ GeV, we also obtain integrated tau-lepton fluxes for $10^6 \leq E/\text{GeV} \leq 10^8$. In this energy range, we can see that the integrated tau-lepton flux from Earth-skimming AGN neutrinos is relatively significant .

In addition to the Earth, the tau-neutrino skims likely through a part of the ocean before exiting the interaction region [27]. Hence, it is important to compare the resulting tau-lepton fluxes as the tau neutrinos skim through mediums with different densities, while the slant depths of mediums are held

Energy Interval	AGN		GRB	
	full	approx	full	approx
$10^6 \leq E/\text{GeV} \leq 10^7$	2.23	2.12	$9.63 \cdot 10^{-3}$	$1.05 \cdot 10^{-2}$
$10^7 \leq E/\text{GeV} \leq 10^8$	4.89	5.12	$7.12 \cdot 10^{-3}$	$6.82 \cdot 10^{-3}$
$10^8 \leq E/\text{GeV} \leq 10^9$	$1.95 \cdot 10^{-1}$	$1.52 \cdot 10^{-1}$	$5.39 \cdot 10^{-4}$	$4.63 \cdot 10^{-4}$
$10^9 \leq E/\text{GeV} \leq 10^{10}$			$1.13 \cdot 10^{-5}$	$1.24 \cdot 10^{-5}$

Energy Interval	GZK	
	full	approx
$10^6 \leq E/\text{GeV} \leq 10^7$	$7.38 \cdot 10^{-5}$	$2.08 \cdot 10^{-5}$
$10^7 \leq E/\text{GeV} \leq 10^8$	$1.14 \cdot 10^{-2}$	$1.90 \cdot 10^{-2}$
$10^8 \leq E/\text{GeV} \leq 10^9$	$8.17 \cdot 10^{-2}$	$8.47 \cdot 10^{-2}$
$10^9 \leq E/\text{GeV} \leq 10^{10}$	$3.31 \cdot 10^{-2}$	$3.52 \cdot 10^{-2}$

Table 2.1: Comparison of the integrated tau-lepton flux ($\text{km}^{-2}\text{yr}^{-1}\text{sr}^{-1}$) in different energy bins for the AGN, the GRB and the GZK neutrinos without and with approximation (see text for details). The distance traversed is taken to be 10 km in rock here. For $10^9 \leq E/\text{GeV} \leq 10^{10}$, the incident AGN neutrino flux is too small so that its induced tau-lepton flux is not shown.

fixed as an example. As pointed out before, the tau-lepton flux is essentially determined by the probability of $\nu_\tau N$ charged-current interaction happening within a tau-lepton range. Furthermore, from Fig. 2.1, it is clear that the tau-lepton range equals to the tau-lepton decay length for E_τ less than 10^7 GeV. One therefore expects $F_\tau^{\text{rock}}(E,X)/F_\tau^{\text{water}}(E,X) = \rho^{\text{rock}}/\rho^{\text{water}}$ for $E_\tau < 10^7$ GeV. This is clearly seen to be the case from Fig. 2.5 and Fig. 2.6, as we compare F_τ^{rock} with $F_\tau^{\text{water}}(E,X)$ for $X = 2.65 \cdot 10^6$ g/cm^2 and $X = 2.65 \cdot 10^7$ g/cm^2 respectively. For $E_\tau > 10^7$ GeV, the tau-lepton range has additional dependencies on the mass density and the atomic number of the medium. Hence the ratio $F_\tau^{\text{rock}}(E,X)/F_\tau^{\text{water}}(E,X)$ starts deviating from $\rho^{\text{rock}}/\rho^{\text{water}}$. It is worthwhile to mention that the tau-lepton flux ratios for AGN and GRB cases behave rather similarly. On the other hand, the ratio in the GZK case has a clear peak between $10^{7.5} < E/\text{GeV} < 10^{8.5}$. Such a peak is even more apparent for the slant depth $X = 2.65 \cdot 10^7$ g/cm^2. The appearance of this peak has to do with the relatively flat behavior of the incident GZK neutrino spectrum, while the position of this peak is related to the energy dependencies of the tau-lepton

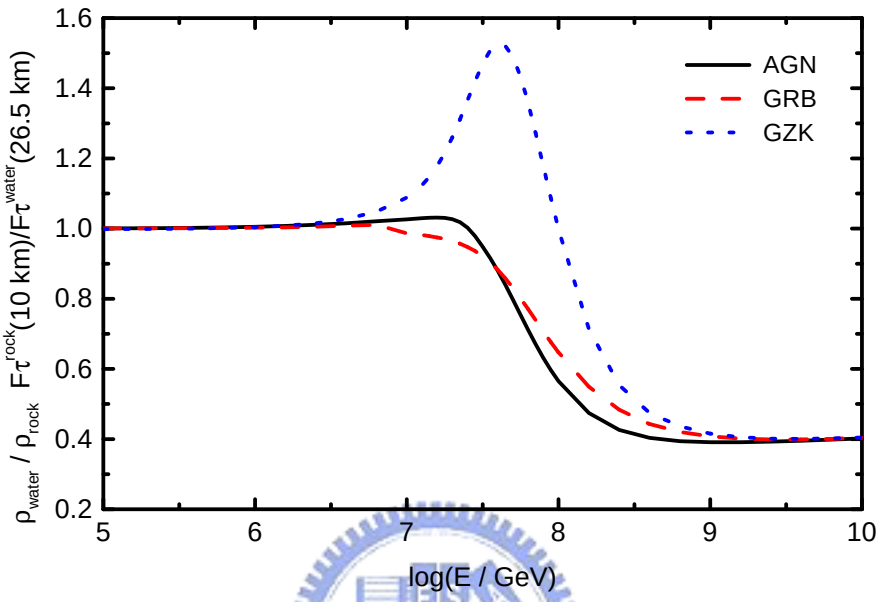

Figure 2.5: The ratio of F_τ in rock and water induced by the AGN, the GRB and the GZK neutrinos for $X = 2.65 \cdot 10^6$ g/cm^2.

range and the neutrino-nucleon scattering cross sections. We have confirmed our observations by computing the flux ratios with simple power-law incident tau-neutrino fluxes. The above peak in the tau-lepton flux ratio implies the suppression of tau-lepton events from ocean-skimming neutrinos compared to those from rock-skimming neutrinos. As stated earlier, the suppression of ocean-skimming neutrinos is related to the spectral index of the incident neutrino flux. It is therefore useful to perform a detailed simulation for it. Such a detailed study is needed because the slant depths traversed by the above two kinds of neutrinos are generally different.

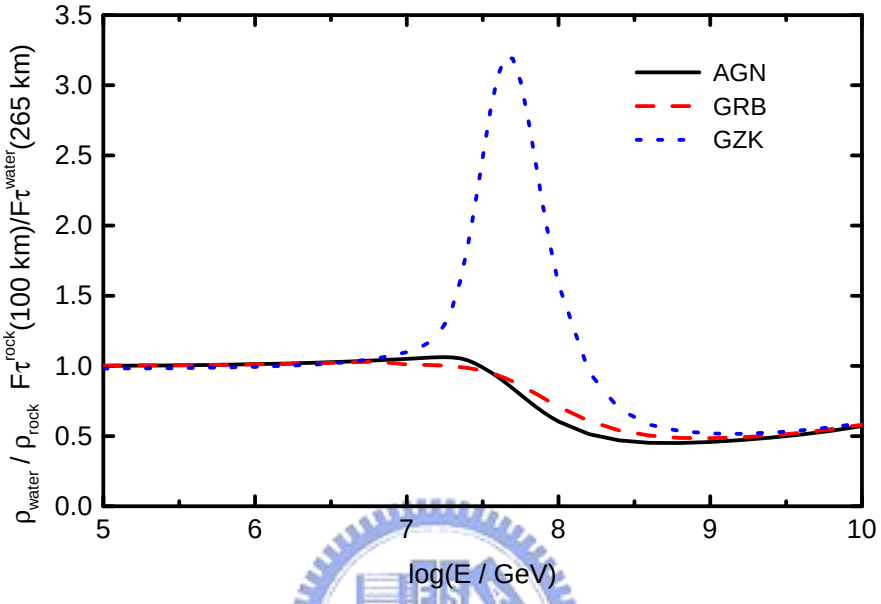

Figure 2.6: The ratio of F_τ in rock and water induced by the AGN, the GRB and the GZK neutrinos for $X = 2.65 \cdot 10^7$ g/cm^2.

2.4 Prospects of possible observations

Because of the expected small flux of the above tau leptons, the detector need the acceptance of the order of $\sim$ km^{2}sr to observe. Concerning the tau-lepton energy spectrum resulting from the AGN neutrinos, it peaks at around 10^7 to 10^8 GeV, which is below the threshold of a fluorescence detector, such as the High Resolution Fly's Eye (HiRes) [28]. Also, these tau leptons come near horizontally. In a short time, it seems very difficult to construct a ground array in vertical direction. A Cherenkov telescope seems to be a feasible solution. In this context, NuTel collaboration is developing Cherenkov telescopes to detect the Earth-skimming high energy neutrinos [27]. Nevertheless, because of the small opening angle of Cherenkov light cone and only a 10% duty cycle (optical

observations are limited to moonless and cloudless nights only), such a detector must cover very large area and field of view. A potential site for NuTel is at Hawaii Big Island, where two large volcanos, namely Mauna Loa and Mauna Kea, could be favorable candidates for high energy neutrinos to interact with. For a detector situated on top of Mount Hualalai and to look at both Mauna Kea and Mauna Loa, the required angular field of view is 8×120. In addition, this telescope should have an acceptance area larger than 2 $\mathrm{km}^2\mathrm{sr}$ so as to detect more than one event per year.

Finally, Let us consider the GZK neutrinos. It is noteworthy that the recent observation of ultra high energy cosmic rays by HiRes seem to be consistent with the GZK cutoff. Hence a future observation of GZK tau neutrinos shall provide a firm support to GZK cutoff. In particular, the slight pile up of tau leptons between 10^8 GeV to 10^9 GeV, induced by the Earth-skimming high energy GZK neutrinos, should be a candidate signature for GZK neutrinos. The integrated tau-lepton flux in this energy range is approximately 0.08 $\mathrm{km}^{-2}\mathrm{sr}^{-1}\mathrm{yr}^{-1}$. To detect one event per year from this flux, the acceptance of a detector must be larger than 120 $\mathrm{km}^2\mathrm{sr}$, for a fluorescence detector (assuming a duty cycle of 10%). Although HiRes can reach 1000 $\mathrm{km}^2\mathrm{sr}$ at energy $> 3 \cdot 10^9$ GeV, it would be a technical challenge to lower down the threshold to 10^8 GeV. Using a system similar to HiRes, the Dual Imaging Cherenkov Experiment (DICE) was able to detect Cherenkov light from extensive air-showers at energy as low as 10^5 GeV [29]. However, the field of view of DICE is also quite small, and thus several Cherenkov telescopes would be needed. An alternative method is a hybrid detection of both Cherenkov and fluorescence photons [30]. That is, a detector similar to HiRes, which looks at both land and sea and detects both Cherenkov and fluorescence photons, may observe the associated signal of GZK neutrinos.

Chapter 3

Tau Neutrino Astronomy in GeV Energies

One of the main motivations for the extra-terrestrial astronomy is to obtain first evidence of tau neutrinos from the cosmos around us above the relatively well known atmospheric neutrino background [31]. The intrinsic fluxes of astrophysical tau neutrinos are generally suppressed compared to those of ν_e and ν_μ. The reason for this flux-hierarchy is due to the production process for the astrophysical neutrinos: $p(\gamma) + p \rightarrow \text{hadrons} \rightarrow \nu + \text{X}$. Since the heavy hadrons that eventually decay into tau neutrinos are not produced as copiously as the light hadrons in the above collisions, the tau neutrino flux is therefore suppressed. However, due to the neutrino mixing suggested by the high-statistics Super-Kamiokande (SK) data, a non-negligible ν_τ flux is expected to reach the Earth. A recent SK analysis of the atmospheric neutrino data implies the following range of the neutrino mixing parameters [32]

$$\Delta m^2_{31} = (1.9 - 3.0) \cdot 10^{-3} \text{ eV}^2, \ \sin^2 2\theta_{23} > 0.9. \tag{3.1}$$

where Δm^2_{31} is the difference in mass squared of the two neutrino mass eigenstates and θ_{23} is the mixing angle. This is a 90% C.L. range with the best fit values given by $\Delta m^2_{31} = 2.4 \cdot 10^{-3}$ eV^2 and $\sin^2 2\theta_{23} = 1$ respectively.

It is to be noted that the tau neutrinos resulting from the above $\nu_\mu \rightarrow \nu_\tau$

oscillations are identified only on the statistical basis (rather than on the event by event basis) [33]. On the other hand, the total number of observed non-tau neutrinos from various detectors are already greater than $\sim 10^4$ with energies ranging from $\sim 10^{-1}$ GeV to $\sim 10^3$ GeV [34]. It is essential to develop efficient techniques for identifying tau neutrinos [24].

There are two important reasons for observing ν_τ. First, seeing ν_τ confirms the $\nu_\mu \to \nu_\tau$ oscillation interpretation for the atmospheric neutrino data. Second, since the atmospheric ν_τ flux is generally suppressed compared to the atmospheric ν_μ flux, the observation of astrophysical ν_τ suffers `much less` background than in the ν_μ case. In this chapter, we address the second point with galactic-plane tau neutrinos as our illustrating astrophysical source. The idea for such an investigation has appeared earlier in Ref. [35].

In the context of two neutrino flavors, ν_μ and ν_τ, the total tau neutrino flux arriving at the detector on Earth, after traversing a distance L, is

$$\phi_{\nu_\tau}^{\rm tot}(E) = P(E) \cdot \phi_{\nu_\mu}(E) + (1 - P(E)) \cdot \phi_{\nu_\tau}(E), \tag{3.2}$$

where $P(E) \equiv P(\nu_\mu \to \nu_\tau) = \sin^2 2\theta_{23} \cdot \sin^2(L/L_{\rm osc})$ is the $\nu_\mu \to \nu_\tau$ oscillation probability, assuming a vanishing θ_{13}, with the neutrino oscillation length given by $L_{\rm osc} = 4E/\Delta m^2_{31}$.

For the sake of computing the total ν_τ flux from a given astrophysical site (including the Earth atmosphere), we need to first compute the intrinsic ν_μ as well as the intrinsic ν_τ flux from the same site.

3.1 Galactic-Plane Neutrino Flux

To calculate the intrinsic galactic-plane ν_μ and ν_τ fluxes, we consider the collisions of incident cosmic-ray protons with the interstellar medium. The following formula is used for computing the fluxes

$$\phi_\nu(E) \;\; = \;\; \int_E^\infty {\rm d}E_p \; \phi_p(E_p) \; f(E_p) \frac{1}{\sigma_{pp}(E_p)} \frac{{\rm d}\sigma_{pp\to\nu+Y}(E_p, E)}{{\rm d}E} \; , \tag{3.3}$$

where E_p denotes the energy of the incident cosmic-ray proton, σ_{pp} is the total inelastic cross section for pp scatterings and $\mathrm{d}\sigma_{pp\to\nu+Y}/\mathrm{d}E$ is the ν energy spectrum in the pp collisions. The function $f(E_p)$ is defined as $f(E_p) \equiv R/\lambda_{pp}(E_p)$, where $\lambda_{pp}(E_p) = \big(n_p\ \sigma_{pp}(E_p)\big)^{-1}$ is the pp interaction length and R is the typical distance in the galaxy along the galactic plane. The target particles are taken to be protons with a constant number density $n_p = 1\ \mathrm{cm}^{-3}$ and R is taken to be ~ 10 kpc, where 1 pc $\simeq 3 \times 10^{18}$ cm. The primary cosmic-ray proton flux, $\phi_p(E_p) \equiv \mathrm{d}N_p/\mathrm{d}E_p$, is given by [36]

$$\phi_p(E_p) = 1.49 \cdot \Big(E_p + 2.15 \cdot \exp(-0.21\sqrt{E_p})\Big)^{-2.74}, \tag{3.4}$$

in units of $\mathrm{cm}^{-2}\mathrm{s}^{-1}\mathrm{sr}^{-1}\mathrm{GeV}^{-1}$. Since the high-energy incoming protons traverse a distance R much shorter than the proton interaction length λ_{pp}, the above flux is under the assumption that the cosmic-ray flux spectrum in the galaxy is a constant and equal to its locally observed value. The galactic-plane neutrino flux is sometimes also referred to as the galactic center region neutrino flux, the galactic disk neutrino flux or the Milky Way neutrino flux. We shall estimate here the neutrino flux coming from the galactic-plane direction only as transverse to it, the $n_p$decreases essentially exponentially [37], and so does the $\phi_\nu(E)$ according to Eq. (3.3). Finally, the neutrino production process $p + p \to \nu + Y$ is mediated by the production and the decays of the π, the K, and the charmed hadrons.

The galactic muon neutrinos mainly come from the two-body π decays and the subsequent three-body muon decays. While the decay rates and the decay distributions of the π and the μ are well understood, the differential cross section for the process $p+p \to \pi+Y$ is model dependent. We adopt the parameterization in [38] for such a cross section, which is obtained by using the accelerator data in the sub-TeV energy range [41]. $F_{N\pi}(E_\pi, E_N)$ is the normalized inclusive cross

section for $N + \text{air} \to \pi^{\pm} + Y$ given by [38]:

$$F_{N\pi}(E_\pi, E_N) \equiv \frac{E_\pi}{\sigma_N}\frac{\mathrm{d}\sigma(E_\pi, E_N)}{\mathrm{d}E_\pi} = c_+(1-x)^{p_+} + c_-(1-x)^{p_-}, \tag{3.5}$$

where $x = E_\pi/E_N$, $c_+ = 0.92$, $c_- = 0.81$, $p_+ = 4.1$, and $p_- = 4.8$. One note that $c_+(1-x)^{p_+}$ corresponds to the π^+ production while $c_-(1-x)^{p_-}$ corresponds to the π^- production. We remark that our galactic-plane ν_μ flux compares well with a previous calculation [37] using the PYTHIA [39]. The galactic-plane ν_τ flux arises from the production and the decays of the D_s mesons. It has been found to be rather suppressed compared to the corresponding ν_μ flux [40].

Because of the relatively suppressed intrinsic ν_τ flux, the total galactic-plane tau neutrino flux, $\phi^{\rm tot}_{\nu_\tau}(E)$, is therefore `dominated` by the $\nu_\mu \to \nu_\tau$ oscillations indicated by the term $P(E) \cdot \phi_{\nu_\mu}(E)$ in Eq. (3.2). With the best-fit values for the neutrino mixing parameters, we have $\phi^{\rm tot}_{\nu_\tau}(E) \approx \phi_{\nu_\mu}(E)/2$, neglecting the contribution of $\phi_{\nu_\tau}(E)$, since $L_{\rm osc} \ll L$, where $L \sim 5$ kpc is the typical average distance traveled by the intrinsic ν_μ after being produced in our galaxy. Finally, the `total` galactic-plane tau neutrino flux, $\phi^{\rm tot}_{\nu_\tau}(E) \equiv \mathrm{d}N/\mathrm{d}(\log_{10}E)$, can be parameterized for 1 GeV $\leq E \leq 10^3$ GeV, as

$$\phi^{\rm tot}_{\nu_\tau}(E) = A\left(\frac{E}{\rm GeV}\right)^{\alpha}, \tag{3.6}$$

where $A = 2 \cdot 10^{-5}$ is in units of $\mathrm{cm}^{-2}\mathrm{s}^{-1}\mathrm{sr}^{-1}$ with $\alpha = -1.64$.

3.2 The Intrinsic Atmospheric Neutrino Fluxes

3.2.1 Intrinsic Atmospheric Muon Neutrino Flux

A. Two-body π, K decays and charmed hadron decays

First of all, we follow the approach in [38] for computing the flux of intrinsic atmospheric muon neutrinos which could oscillate into tau neutrinos. This approach computes the flux of muon neutrinos coming from pion and kaon decays.

For the π-decay contribution, the flux formula reads:

$$\frac{\mathrm{d}^2 N^{\pi}_{\nu_\mu}(E,\xi,X)}{\mathrm{d}E\mathrm{d}X} = \int_E^{\infty} \mathrm{d}E_N \int_E^{E_N} \mathrm{d}E_\pi \frac{\Theta(E_\pi - \frac{E}{1-r_\pi})}{d_\pi E_\pi (1-r_\pi)} \int_0^X \frac{\mathrm{d}X'}{\lambda_N} P_\pi(E_\pi, X, X') \times \frac{1}{E_\pi} F_{N\pi}(E_\pi, E_N) \times \exp\left(-\frac{X'}{\Lambda_N}\right) \phi_N(E_N), \quad (3.7)$$

where E is the neutrino energy and ξ is the zenith angle in the direction of the incident cosmic-ray nucleons. The $\gamma_\pi = m_\mu^2/m_\pi^2$ and d_π is the pion decay length in units of g/cm^2. The λ_N is the nucleon interaction length while Λ_N is the corresponding nucleon attenuation length. $\phi_N(E_N)$ is the primary cosmic-ray spectrum. We only consider the proton component of ϕ_N, which is given by Eq. (3.4).

The function $P_\pi(E_\pi, X, X')$ is the probability that a charged pion produced at the slant depth X' (g/cm^2) survives to the depth X ($> X'$), $F_{N\pi}(E_\pi, E_N)$ is the normalized inclusive cross section for $N + \mathrm{air} \to \pi^\pm + Y$ given by Eq. (3.5). The kaon contribution to the atmospheric ν_μ flux has the same form as Eq. (3.7) with an inclusion of the branching ratio $B(K \to \mu\nu) = 0.635$ and appropriate replacements in kinematic factors and the normalized inclusive cross section. In particular, $F_{NK}(E_K, E_N)$ can be parameterized as Eq. (3.5) with $c_+ = 0.037$, $c_- = 0.045$, $p_+ = 0.87$, and $p_- = 3.5$. Finally the nucleon interaction length, λ_N, and the nucleon attenuation length, Λ_N, are both model dependent. A simplified approach based upon the Feynman scaling render both λ_N and Λ_N energy independent and $Z_{pp} \equiv 1 - \lambda_p/\Lambda_p = 0.263$ [41, 42], whereas a PYTHIA [39] calculation give rise to an energy dependent Z_{pp} [44]. Both results on Z_{pp} are compared in Fig. 3.1 where we have extrapolated the energy dependent $Z_{pp}(E)$ in Ref. [44] down to $E = 1$ GeV. The above two approaches for calculating the hadronic Z moments also give rise to different results for $Z_{\pi\pi}$, Z_{KK}, $Z_{N\pi}$ and Z_{NK}, where the last two Z-moments are related to the productions of pions and kaons by the nucleon-air collisions. In this paper, we shall only study the Z_{pp} dependence of the atmospheric ν_μ flux (and consequently the atmospheric ν_τ flux) since the dependencies of this flux on $Z_{N\pi}$ and Z_{NK} have been studied

in [45]. Furthermore, compared to the Z_{pp} case, the values of $Z_{\pi\pi}$ and Z_{KK} obtained by the Feynman scaling do not differ significantly from those obtained by the PYTHIA calculations, as seen from [44].

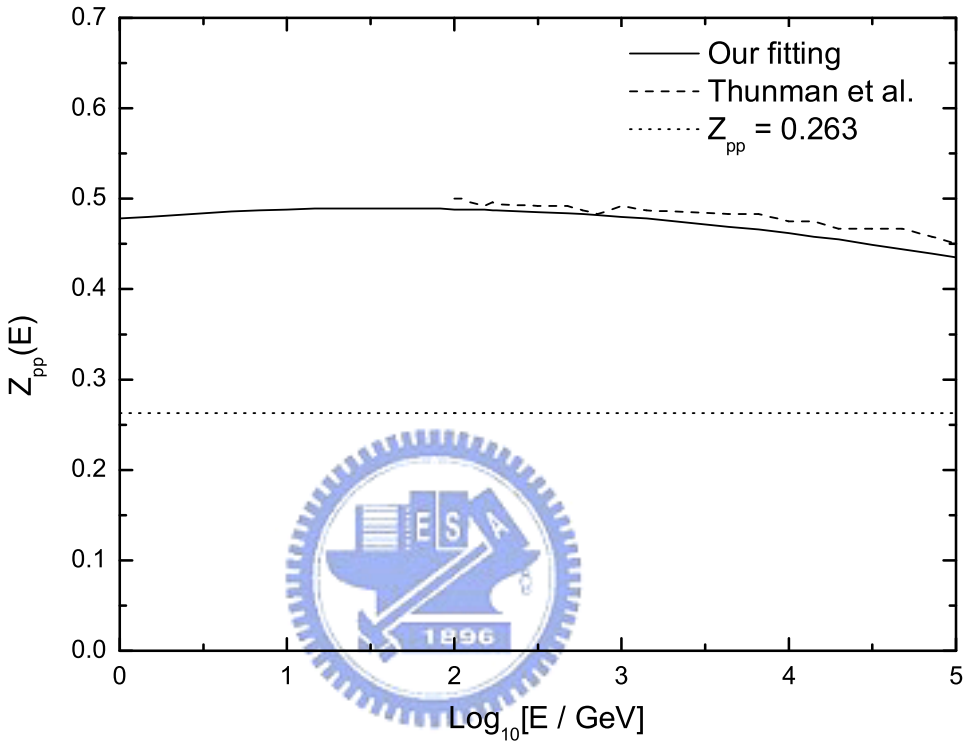

Figure 3.1: The comparison of Z_{pp} obtained by assuming the Feynman scaling [41] and that obtained by PYTHIA [44]. Our extrapolation of the latter result is also shown.

To proceed for calculating $\mathrm{d}^2 N^{\pi}_{\nu_\mu}(E,\xi,X)/\mathrm{d}E\mathrm{d}X$, we note that $P_\pi(E_\pi, X, X')$ is given by [42]

$$P_\pi(E_\pi, X, X') = \exp\left(-\frac{X-X'}{\Lambda_\pi}\right)\cdot\exp\left(-\frac{m_\pi c}{\tau_\pi}\int_{X'}^{X}\frac{\mathrm{d}T}{\rho(T)}\right), \tag{3.8}$$

where $\Lambda_\pi = 160$ g/cm^2 is the pion attenuation constant, τ_π is the pion lifetime at its rest frame, while $\rho(T)$ is the atmosphere mass density at the slant depth

T. For $\xi \leq 60^\circ$, the curvature of the Earth can be neglected so that $\rho(T) = T\cos\xi/h_0$ with $h_0 = 6.4$ km the scale height for an exponential atmosphere. In this approximation, the above survival probability can be written as [38]

$$P_\pi(E_\pi, X, X') = \exp\left(-\frac{X - X'}{\Lambda_\pi}\right) \cdot \left(\frac{X'}{X}\right)^{\epsilon_\pi / E_\pi \cos\xi}, \tag{3.9}$$

where $\epsilon_\pi = m_\pi c^2 h_0 / c\tau_\pi$ is the pion decay constant. Depending on the zenith angle, we apply either Eq. (3.8) or Eq. (3.9) to perform the calculations. The kaon survival probability $P_K(E_K, X, X')$ has the same form as $P_\pi(E_\pi, X, X')$ except replacing Λ_π with Λ_K and ϵ_π with ϵ_K. The two-body π and K decay contribution to the atmospheric ν_μ flux is given by the sum of $\mathrm{d}^2 N^\pi_{\nu_\mu}(E, \xi, X)/\mathrm{d}E\mathrm{d}X$ and $\mathrm{d}^2 N^K_{\nu_\mu}(E, \xi, X)/\mathrm{d}E\mathrm{d}X$.

Let us consider the charm-decay contribution to the atmospheric ν_μ flux. For $E > 10^6$ GeV, the charm-decay contribution becomes more important than those of the π and the K decays. We have used the results from the perturbative QCD to estimate this contribution [54]. The muon neutrino flux due to charm contribution can be written as

$$\frac{\mathrm{d}^2 N^c_{\nu_\mu}(E, X)}{\mathrm{d}E\mathrm{d}X} = \sum_h \frac{Z_{ph} Z_{h\nu_\mu}}{1 - Z_{pp}(E)} \cdot \frac{\exp(-X/\Lambda_p)\phi_p(E)}{\Lambda_p}, \tag{3.10}$$

where h stands for the $D^\pm$, the D^0, the D_s and the Λ_c hadrons. The Z moments on the RHS of the equation are defined by

$$Z_{ij}(E_j) \equiv \int_{E_j}^\infty \mathrm{d}E_i \frac{\phi_i(E_i)}{\phi_i(E_j)} \frac{\lambda_i(E_j)}{\lambda_i(E_i)} \frac{\mathrm{d}n_{iA\to jY}(E_i, E_j)}{\mathrm{d}E_j}, \tag{3.11}$$

with $\mathrm{d}n_{iA\to jY}(E_i, E_j) \equiv \mathrm{d}\sigma_{iA\to jY}(E_i, E_j)/\sigma_{iA}(E_i)$. In the decay process, the scattering length λ_i is replaced by the decay length d_i while the $\mathrm{d}n_{iA\to jY}(E_i, E_j)$ is replaced by the $\mathrm{d}\Gamma_{i\to jY}(E_i, E_j)/\Gamma_i(E_i)$. We note that this part of the atmospheric ν_μ flux is isotropic, unlike the contributions from the π and the K decays. Such a difference is attributable to the lifetime difference between the charm and the $\pi(K)$ mesons. The charm hadrons decay into neutrinos before interacting in the atmosphere. Hence the depth of the atmosphere, varied according to different directions of charm hadrons, has no effect on the

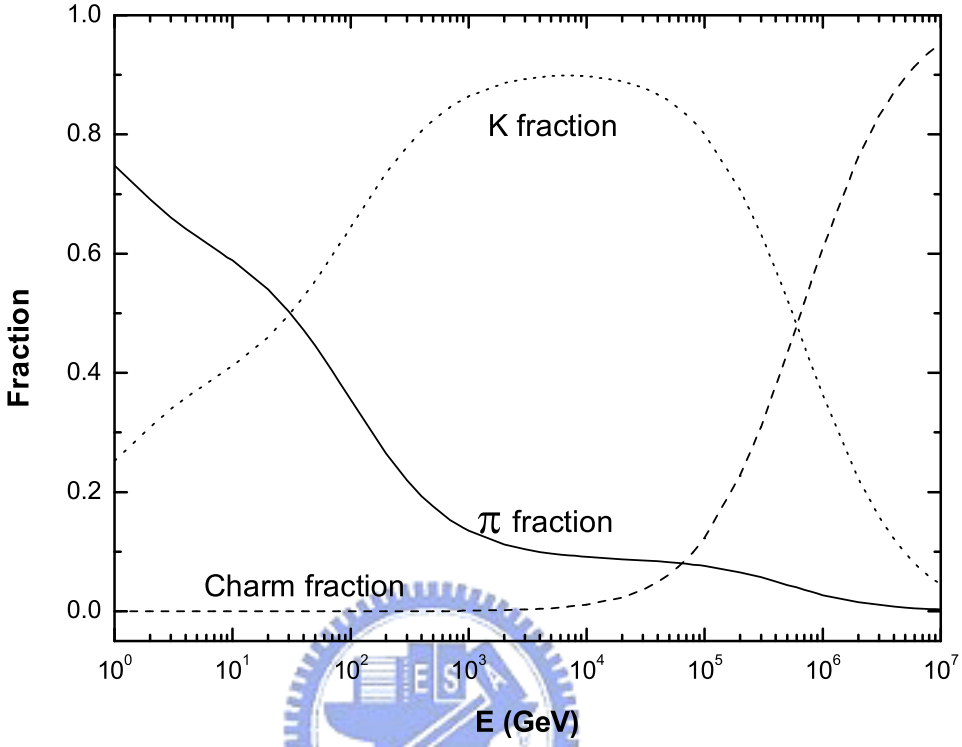

Figure 3.2: The fraction of contributions by the π, the K, and the charm decays to the overall downward going atmospheric ν_μ flux(neglects the 3-body muon-decay contribution) as a function of the neutrino energy in GeV.

resulting neutrino spectrum. To determine Z_{ph}, it is necessary to calculate $\mathrm{d}\sigma_{pA\to hY}(E_p, E_h)/\mathrm{d}E_h$. The next-to-leading order (NLO) perturbative QCD [46, 47] is employed to calculate the differential cross section of $pA \to c\bar{c}$, and an appropriate probability factor is appended to account for each fragmentation process $c \to H$ [54]. Finally the decay moments $Z_{h\nu_\mu}$ are calculated by using the charmed-hadron decay distributions given in Refs. [48, 42].

It is instructive to see the relative contribution by the π, the K, and the charm decays to the overall ν_μ flux which neglects the 3-body muon-decay contribution. In Fig. 3.2, we show the relative contributions by the π, the K, and

the charm decays to the overall ν_μ flux(neglects the 3-body muon-decay contribution). This is an extension of the Fig. 3 in Ref. [38], where only the π and the K contributions are compared. It is easily seen that the π decay contribution dominates for 1 GeV $\leq E \leq$ 10 GeV, while the K decay contribution dominates between 10^3 GeV and 10^5 GeV. The fraction of the charm-decay contribution rises rapidly at $E \geq 10^5$ GeV and becomes dominant for $E > 10^6$ GeV. In this energy range, both the π and the K lose large fractions of their energies before decaying into the neutrinos.

B. Three-body μ decays

We recall that Eq. (3.7) and its corresponding form in the kaon decay case only calculate the flux of muon neutrinos arising from two-body pion and kaon decays. To calculate the contribution from three-body muon decays, it is useful to first obtain the muon flux [38]:

$$\begin{aligned}\frac{\mathrm{d}N_\mu^\pi(E,\xi,X)}{\mathrm{d}E} &= \int_{E'}^{\infty}\mathrm{d}E_N\int_{E'}^{E_N}\mathrm{d}E_\pi\int_0^X \mathrm{d}X^{''}P_\mu(E,X,X^{''}) \\ &\times \frac{\Theta(E_\pi-E')\Theta(\frac{E'}{r_\pi}-E_\pi)}{d_\pi E_\pi(1-r_\pi)}\times\int_0^{X^{''}}\frac{\mathrm{d}X'}{\lambda_N}P_\pi(E_\pi,X^{''},X') \\ &\times \frac{1}{E_\pi}F_{N\pi}(E_\pi,E_N)\times\exp\left(-\frac{X'}{\Lambda_N}\right)\phi_N(E_N), \qquad (3.12)\end{aligned}$$

where E' and E are muon energies at slant depths $X^{''}$ and X respectively, while $P_\mu(E,X,X^{''})$ is the muon survival probability given by [42]

$$P_\mu(E,X,X^{''}) = \exp\left[-\frac{m_\mu c}{\tau_\mu}\int_{X''}^{X}\mathrm{d}T\frac{1}{E(T-X'',E')\rho(T)}\right], \qquad (3.13)$$

where τ_μ is the muon lifetime at its rest frame and $E(T-X^{''},E')$ is the muon energy at the slant depth T with E' the muon energy at its production point $X^{''}$. In the Earth's atmosphere, only the ionization process [49] is important for the muon energy loss so that

$$E(T-X^{''},E') = E' - \alpha(T-X^{''}), \qquad (3.14)$$

with $\alpha \approx 2$ MeV/g/cm^2 characterizing the muon ionization loss in the medium. For the zenith angle $\xi \leq 60^\circ$, the above survival probability can be written as [38]

$$P_\mu(E, X, X^{''}) = \left(\frac{X^{''}}{X} \frac{E}{E + \alpha(X - X^{''})} \right)^{\epsilon_\mu/(E\cos\xi + \alpha X \cos\xi)}, \tag{3.15}$$

with $\epsilon_\mu = m_\mu c^2 h_0 / c\tau_\mu$ the muon decay constant. Since the muons are polarized, it is convenient to keep track of the right-handed and left-handed muon fluxes separately. The probability for a produced μ^- to be right-handed or left-handed is determined by the muon polarization [50, 51]:

$$P_\mu(x) = \frac{1 + r_\pi}{1 - r_\pi} - \frac{2r_\pi}{(1 - r_\pi)x}, \tag{3.16}$$

with $x = E_\mu/E_\pi$ and $r_\pi = m_\mu^2/m_\pi^2$. Hence $P_{R,L}(x) = \frac{1}{2}(1 \pm P_\mu(x))$ are the probabilities for the produced muon to be right-handed or left-handed respectively. The polarization for μ^+ has an opposite sign to that of μ^-. The probabilities $P_{R,L}(x)$ should be inserted into Eq. (3.12) for obtaining four different components of the muon flux: $\mathrm{d}N^\pi_{\mu^+_R}/\mathrm{d}E$, $\mathrm{d}N^\pi_{\mu^-_R}/\mathrm{d}E$, $\mathrm{d}N^\pi_{\mu^+_L}/\mathrm{d}E$, and $\mathrm{d}N^\pi_{\mu^-_L}/\mathrm{d}E$. There are additional four components of the muon flux arising from the kaon decays. The calculation of these components proceeds in the same way as the pion decay case. The ν_μ flux resulting from the muon flux is then given by [42]

$$\frac{\mathrm{d}^2 N^{\mu^\pm}_{\nu_\mu}(E, \xi, X)}{\mathrm{d}E\mathrm{d}X} = \sum_{s=L,R} \int_E^\infty \mathrm{d}E_\mu \frac{F_{\mu^\pm_s \to \nu_\mu}(E/E_\mu)}{d_\mu(E_\mu, X)E_\mu} \cdot \frac{\mathrm{d}N_{\mu^\pm_s}(E_\mu, \xi, X)}{\mathrm{d}E_\mu}, \tag{3.17}$$

where $d_\mu(E_\mu, X)$ is the muon decay length in units of g/cm^2 at the slant depth X and $F_{\mu^\pm_s \to \nu_\mu}(E/E_\mu)$ is the decay distribution of $\mu^\pm_s \to \nu_\mu$. Precisely, in the ultra-relativistic limit, one has [42]

$$F_{\mu^- \to \nu_\mu}(y) = g_0(y) + P_\mu g_1(y), \tag{3.18}$$

with $g_0(y) = 5/3 - 3y^2 + 4y^3/3$, $g_1(y) = 1/3 - 3y^2 + 8y^3/3$. We generally do not include the charm-hadron decay contribution to the muon neutrino flux. It is shown in Fig. 3.2 that charm-hadron decays contribute less than 5% to the overall muon neutrino flux for $E_\nu < 10^5$ GeV.

3.2.2 Intrinsic Atmospheric Tau Neutrino Flux

After finishing the calculation of the intrinsic atmospheric muon neutrino flux, we also need to calculate the intrinsic atmospheric tau neutrino flux to completely determine the total one. Since the flux of intrinsic atmospheric tau neutrino arises from D_s decays, one calculates its flux by solving the following cascade equations [41]:

$$\begin{aligned}
\frac{\mathrm{d}\phi_p(E,X)}{\mathrm{d}X} &= -\frac{\phi_p}{\lambda_p} + Z_{pp}\frac{\phi_p}{\lambda_p} \\
\frac{\mathrm{d}\phi_{D_s}(E,X)}{\mathrm{d}X} &= -\frac{\phi_{D_s}}{\lambda_{D_s}} - \frac{\phi_{D_s}}{d_{D_s}} + Z_{pD_s}\frac{\phi_p}{\lambda_p} + Z_{D_sD_s}\frac{\phi_{D_s}}{\lambda_{D_s}} \\
\frac{\mathrm{d}\phi_{\nu_\tau}(E,X)}{\mathrm{d}X} &= Z_{D_s\nu_\tau}\frac{\phi_{D_s}}{d_{D_s}},
\end{aligned} \tag{3.19}$$

where the particle flux $\mathrm{d}\phi_i(E,X)/\mathrm{d}X$ denotes $\mathrm{d}^2N_i(E,X)/\mathrm{d}E\mathrm{d}X$, d_i and λ_i denote particle's decay and interaction length in g/cm^2 respectively, and the Z moments Z_{ij} are defined in Eq. (3.11). In our concerned energy range, the chain of equations in (3.19) can be solved easily by simplifying the second equation, namely by neglecting terms ϕ_{D_s}/λ_{D_s} and $Z_{D_sD_s}\phi_{D_s}/\lambda_{D_s}$. One obtains

$$\frac{\mathrm{d}^2N_{\nu_\tau}(E,X)}{\mathrm{d}E\mathrm{d}X} = \frac{Z_{pD_s}Z_{D_s\nu_\tau}}{1-Z_{pp}(E)}\cdot\frac{\exp(-X/\Lambda_p)\phi_p(E)}{\Lambda_p}, \tag{3.20}$$

We use two different values for $Z_{pp} \equiv 1 - \lambda_p/\Lambda_p$ as shown in Fig. 3.1. To determine Z_{pD_s}, it is necessary to calculate $\mathrm{d}\sigma_{pA\to D_sY}(E_p,E_{D_s})/\mathrm{d}E_{D_s}$. Since D_s meson is heavy enough, the above differential cross section is calculable using perturbative QCD [53]. In this work, the next-to-leading order (NLO) perturbative QCD [46, 47] with CTEQ6 parton distribution functions [17] are employed to calculate the differential cross section of $pA \to c\bar{c}$. To obtain $\mathrm{d}\sigma_{pA\to D_sY}(E_p,E_{D_s})/\mathrm{d}E_{D_s}$, we multiply the charm quark differential cross section by the probability factor 13% to account for the fragmentation process $c \to D_s$ [53]. In Fig. 3.3, we compare our Z_{pD_s} to a previous result obtained by the CTEQ3 parton distribution functions [54]. In the latter work, the NLO

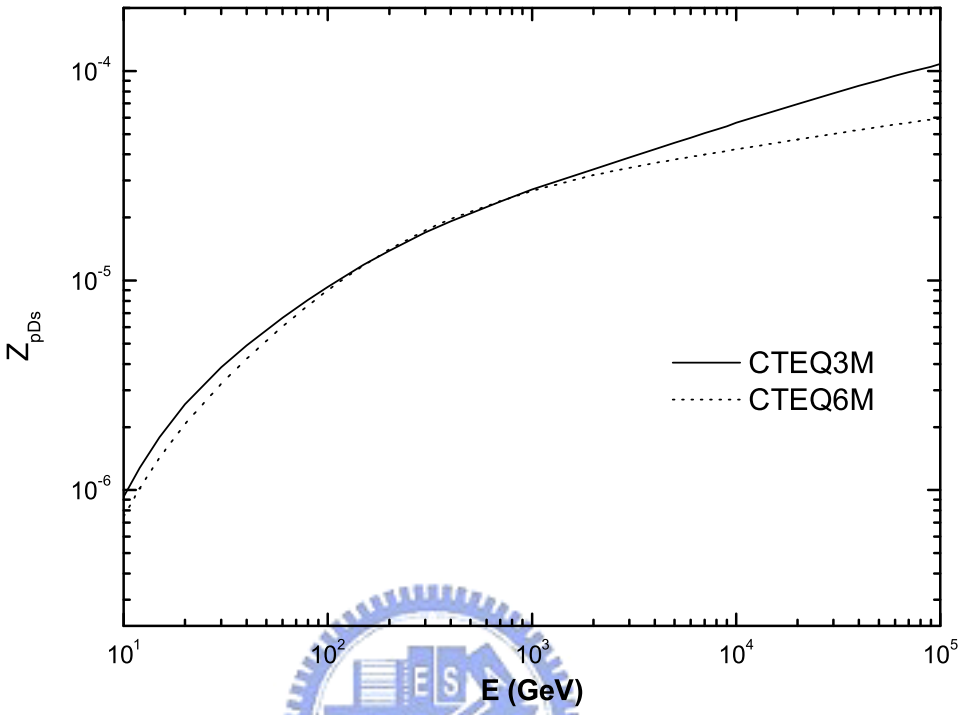

Figure 3.3: The Z moment Z_{pD_s} obtained by perturbative QCD with CTEQ3 and CTEQ6 parton distribution functions respectively.

pertubative QCD effects are taken into account by the K factor defined by

$$K(E, x_E) = \frac{\mathrm{d}\sigma^{\mathrm{NLO}}/\mathrm{d}x_E}{\mathrm{d}\sigma^{\mathrm{LO}}/\mathrm{d}x_E}, \tag{3.21}$$

where $\mathrm{d}\sigma^{\mathrm{LO}}/\mathrm{d}x_E$ and $\mathrm{d}\sigma^{\mathrm{NLO}}/\mathrm{d}x_E$ are leading order and next-to-leading order differential cross sections for $pA \to c\bar{c}$ respectively, with $x_E = E_c/E_p$. For QCD renormalization scale $\mu = m_c$ and the factorization scale $M = 2m_c$, the K factor is fitted to be [54]

$$\begin{aligned} K(E, x_E) &= 1.36 + 0.42 \ln\left(\ln(E/\mathrm{GeV})\right) \\ &+ \left(3.40 + 18.7(E/\mathrm{GeV})^{-0.43} - 0.079 \ln(E/\mathrm{GeV})\right) x_E^{1.5}. \end{aligned} \tag{3.22}$$

We apply this K factor to our calculation with CTEQ6 parton distribution functions. Comparing this result with that obtained by applying CTEQ3 parton distribution functions, one acquires an idea on the uncertainty of perturbative QCD approach to the charm hadron production cross section. It is seen from Fig. 3.3 that both Z moments agree well for energies below TeV. For $E = 10^4$ GeV, they differ by about 30%.

In addition to perturbative QCD approach, there are non-perturbative approach for computing the charm hadron production cross section. In fact, such non-perturbative approaches [55, 56] are motivated to accommodate accelerator data on strange particle productions, which are underestimated by the perturbative QCD approach. It is desirable to apply these approaches to charm hadron productions. The quark-gluon-string-model (QGSM) [55] is a non-perturbative approach based upon the string fragmentation, where the model parameters are tuned to the strange particle productions. The recombination-quark-parton-model (RQPM) [56] is also a phenomenological approach which takes into account the contribution of the intrinsic charm in the nucleon to the charm hadron production cross section. Detailed comparisons of these two models with perturbative QCD approach on the charm hadron productions are given in [57]. It is shown that perturbative QCD approach gives the smallest charm production Z moments. It is clear that the model dependencies on the charm hadron productions affect both the prompt atmospheric muon neutrino flux and the intrinsic atmospheric tau neutrino flux. A detailed study on the model dependencies of the intrinsic atmospheric tau neutrino flux is given in [58]. We shall further discuss these model dependencies after the discussion on the Z moment $Z_{D_s\nu_\tau}$.

It is noted that $Z_{D_s\nu_\tau}$ is related to the energy distributions of the D_s decays into tau neutrinos. One arises from the decay $D_s \to \nu_\tau\tau$, and the other follows from the subsequent tau-lepton decay, $\tau \to \nu_\tau + X$. The latter contribution is calculated using the decay distributions of the decay modes $\tau \to \nu_\tau\rho$, $\tau \to \nu_\tau\pi$, $\tau \to \nu_\tau a_1$ [59, 53], and $\tau \to \nu_\tau l\nu_l$ [41, 42].

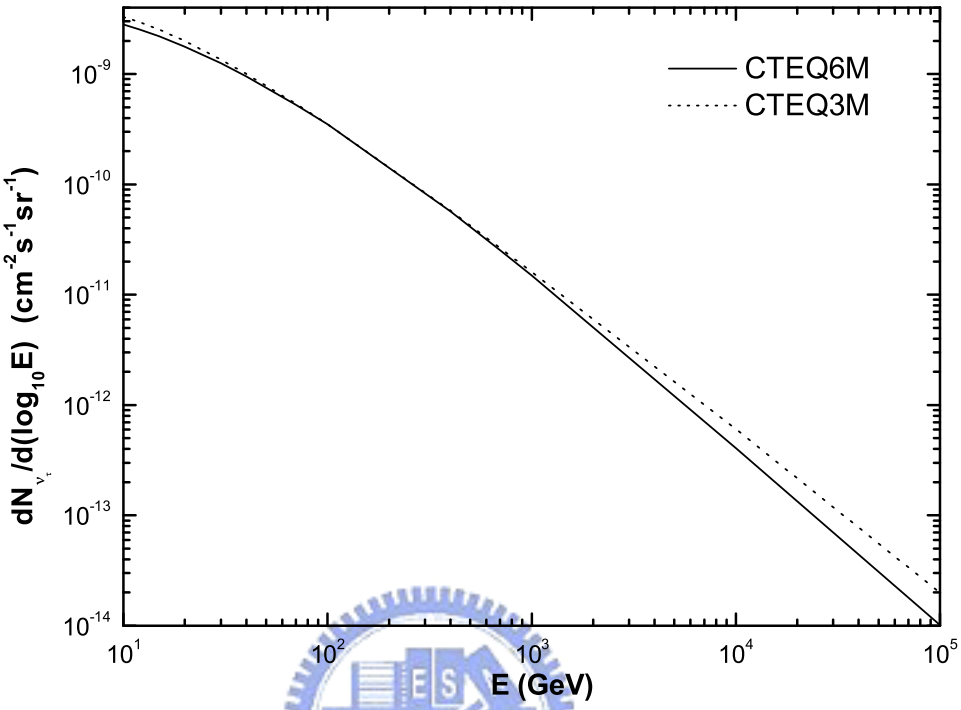

Figure 3.4: The comparison of intrinsic atmospheric ν_τ fluxes calculated by perturbative QCD with CTEQ3 and CTEQ6 parton distribution functions respectively.

It is negligible for the uncertainty of intrinsic atmospheric ν_τ flux due to different approaches for Z_{pp}. The main uncertainty of this flux is due to the model dependence of the Z-moment Z_{pD_s}. Within the perturbative QCD approach, the dependence of this flux on the parton distribution functions is shown in Fig. 3.4. It is easily seen that the intrinsic atmospheric ν_τ flux is not sensitive to parton distribution functions for $E < 10^3$ GeV. However, at $E = 10^4$ GeV, both fluxes differ by almost 50%. Incorporating the non-perturbative approaches for charm hadron productions [55, 56], the uncertainties of intrinsic atmospheric ν_τ flux is depicted in Fig. 3.5. It is seen that the minimal ν_τ flux in Ref. [58] is consistent with our ν_τ flux calculated by perturbative QCD with CTEQ6

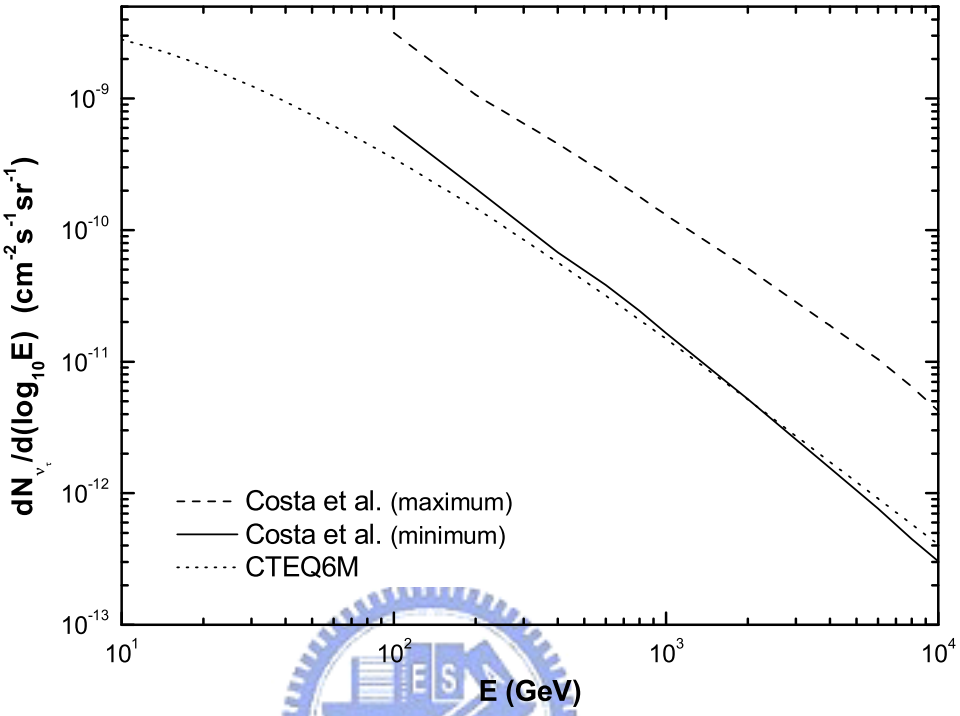

Figure 3.5: The model dependencies of intrinsic atmospheric ν_τ flux. The minimal fluxes from Ref. [58] is given by perturbative QCD. The maximum flux from the same reference is given by RQPM model for $E \leq 300$ GeV, and by QGSM model for $E > 300$ GeV

parton distribution functions. On the other hand, the maximal flux shown in Fig. 3.5 is almost one order of magnitude larger than the minimal one. This maximal flux is given by the RQPM model below 300 GeV while it is given by the QGSM model beyond this energy [60]. We remark that the original minimal and maximal ν_τ fluxes in Ref. [58] correspond to different sets of primary cosmic ray flux, which is considered as one of the uncertainties for the ν_τ flux. However, we have re-scaled these fluxes to a common cosmic ray flux, Eq. (3.4), used in this paper. We also note that the uncertainty of intrinsic atmospheric ν_τ flux provided by Ref. [58] starts at $E = 100$ GeV, while our calculation of

this flux starts at $E = 10$ GeV.

We are interested in seeing how much the uncertainty of the intrinsic ν_τ flux could affect the determination of the ν_τ flux taking into account the oscillation effect. In the next section, we shall study this issue with respect to the upward atmospheric ν_τ flux where the oscillation effect is the largest.

3.3 The Atmospheric Tau Neutrino Flux With Oscillations In The Two-Flavor Mixing Scheme

3.3.1 The Downward and Horizontal Atmospheric Tau Neutrino Fluxes

The following formula is used for calculating the atmospheric tau neutrino flux

$$\frac{\mathrm{d}\bar{N}_{\nu_\tau}(E,\xi)}{\mathrm{d}E} = \int_0^{X_{\max}(\xi)} \mathrm{d}X \left[\frac{\mathrm{d}^2 N_{\nu_\mu}(E,\xi,X)}{\mathrm{d}E\mathrm{d}X} \cdot P_{\nu_\mu \to \nu_\tau}\left(E, L(X,\xi)\right) + \frac{\mathrm{d}^2 N_{\nu_\tau}(E,\xi,X)}{\mathrm{d}E\mathrm{d}X} \cdot \left(1 - P_{\nu_\mu \to \nu_\tau}\left(E, L(X,\xi)\right)\right) \right], \quad (3.23)$$

where $P_{\nu_\mu \to \nu_\tau}\left(E, L(X,\xi)\right) \equiv \sin^2 2\theta_{23} \sin^2(1.27\Delta m^2_{31} L/E)$ is the $\nu_\mu \to \nu_\tau$ oscillation probability, assuming a vanishing θ_{13}, and L is the linear distance from the neutrino production point to the detector on the Earth. For $\xi \leq 60^\circ$, the curvature of the Earth can be neglected so that $L(X,\xi) = -h_0 \ln(X\cos\xi/X_0)/\cos\xi$ with $X_0 = 1030$ g/cm^2 and $h_0 = 6.4$ km. We have used the notation $\frac{\mathrm{d}\bar{N}_{\nu_\tau}(E,\xi)}{\mathrm{d}E}$ to denote the atmospheric ν_τ flux taking into account the oscillation effect. The unit of Δm^2_{31} is eV^2 while L and E are in units of km and GeV respectively. The range of Δm^2_{31} and $\sin^2 2\theta_{23}$ have been given in Eq. (3.1) with the best fit values given by $\Delta m^2_{31} = 2.4 \cdot 10^{-3}$ eV^2 and $\sin^2 2\theta_{23} = 1$ respectively.

A. Meson decay contributions

Using the best fit values of neutrino oscillation parameters, we obtain atmospheric tau neutrino fluxes for $\cos\xi = 0.2,\ 0.4,\ \cdots,\ 1$ as depicted in Fig. 3.6. This set of result is obtained by using an energy-independent Z moment, $Z_{pp} \equiv 1 - \lambda_p/\Lambda_p =$

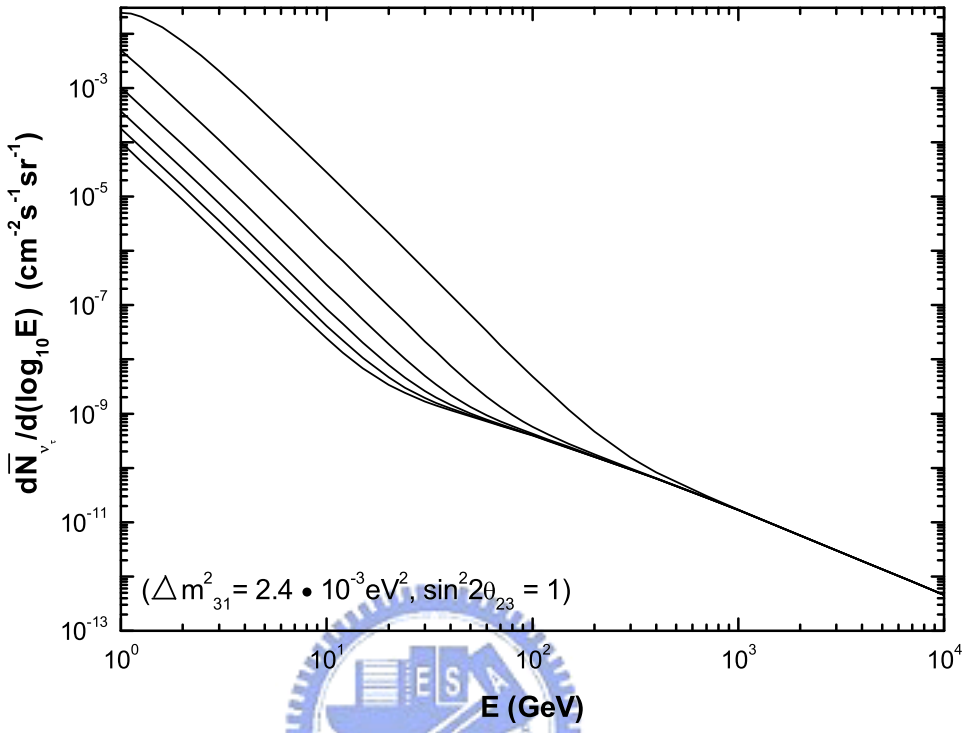

Figure 3.6: The atmospheric ν_τ flux for $\cos\xi = 0$, 0.2, 0.4, 0.6, 0.8 and 1 (from top to bottom) with $\sin^2 2\theta_{23} = 1$, $\Delta m^2_{31} = 2.4 \cdot 10^{-3}$ eV^2, and $Z_{pp} = 0.263$.

0.263 mentioned earlier. For the ν_μ flux on the R.H.S. of Eq. (3.23), we only include the two-body pion and kaon decay contributions. The muon-decay contribution to this flux will be presented later. The intrinsic ν_τ flux in the same equation is taken to be that calculated by perturbative QCD with CTEQ6 parton distribution functions [17]. We note that the atmospheric ν_τ flux increases as ξ increases from 0° to 90°. There are two crucial factors dictating the angular dependence of such a flux. First, the atmosphere depth traversed by the cosmic ray particles increases as the zenith angle ξ increases. Second, the atmospheric muon neutrinos are on-average produced more far away from the ground detector for a larger zenith angle, implying a larger $\nu_\mu \to \nu_\tau$ oscillation probability.

In fact, the neutrino path-length dependencies on the zenith angle ξ and the neutrino energy E_ν have been studied carefully by the Monte-Carlo simulation [61]. Our semi-analytic approach reproduces these dependencies very well. In

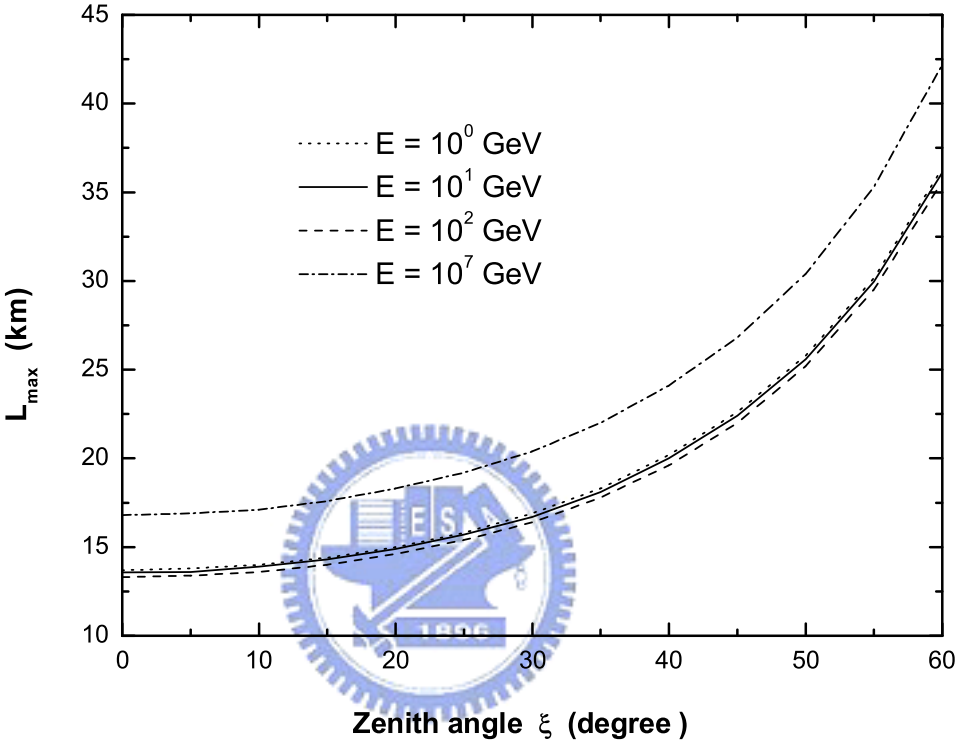

Figure 3.7: The linear distance between the earth detector and the position for maximum ν_μ production in the atmosphere as a function of incident neutrino zenith angle.

Fig. 3.7, we show that $L_{\max}$(the linear distance between the earth detector and the position for maximum ν_μ production in the atmosphere) increases with the incident neutrino zenith angle ξ. Since the $L_{\max}$ nearly equals to the average neutrino path-length from the ν_μ production point to the ground detector, it is found that, for $E_\nu = 10$ GeV and $\cos\xi = 1$ ($\xi = 0°$), the average neutrino path-length is $\sim$ 14 km from Fig. 3.7. The average neutrino path-length in-

creases to 36 km and 650 km for $\xi = 60^\circ$ and $\xi = 90^\circ$ (not included in Fig. 3.7) respectively. The huge path-length of horizontal neutrinos makes the ν_τ flux in this direction two orders of magnitude larger than the downward ν_τ flux. It is also interesting to note that the horizontal ν_τ flux for E_ν approaching 1 GeV begins to show oscillatory behavior. This is because, for $E_\nu = 1$ GeV and $\Delta m^2_{31} = 2.4 \cdot 10^{-3}$ eV^2, $L_{\rm osc} \equiv 4E_\nu/\Delta m^2_{31} \approx 330$ km which is already shorter than the average neutrino path-length at this zenith angle.

It is necessary to emphasize that our calculation procedures for $\cos\xi > 0.5$ and $\cos\xi < 0.5$ are different. In the former case, the curvature of the Earth can be neglected and the pion or kaon survival probability in the atmosphere is approximated by Eq. (3.9). This is the approach we adopted in Ref. [52]. For $\cos\xi < 0.5$, i.e., $\xi > 60^\circ$, we use Eq. (3.8) for the meson survival probability. In this case the calculation is much more involved as the meson survival probability in Eq. (3.8) contains an additional integration. It has been pointed out in Ref. [61] that one may apply Eq. (3.9) for calculating the path-length distribution of neutrinos for $\xi > 60^\circ$ so long as one replaces $\cos\xi$ by $\cos_{\rm eff}\xi$, where the latter is a fitted function of the former. Precisely speaking, by fitting the analytic calculation based upon Eq. (3.9) [42] to the Monte-Carlo calculation, the relations between $\cos\xi$ and $\cos_{\rm eff}\xi$ can be found, which are tabulated in [61]. Extrapolating such a relation, we find that $\cos_{\rm eff}\xi = 0.05$ for $\cos\xi = 0$. Using this $\cos_{\rm eff}\xi$ with Eq. (3.9), we also calculate the atmospheric ν_τ flux. The result is compared with that obtained by the full calculation (applying Eq. (3.8)) as shown in Fig. 3.8. Both results agree very well. Such an agreement makes our calculation compelling and also validates the above extrapolation on $\cos_{\rm eff}\xi$.

It is noteworthy that we have so far computed the atmospheric neutrino flux with an energy independent Z moment, $Z_{pp} \equiv 1 - \lambda_p/\Lambda_p = 0.263$. It is important to check the sensitivity of atmospheric ν_τ flux on the values of Z_{pp}. We recall that different results for Z_{pp} are shown in Fig. 3.1. At energies between 10^2 GeV and 10^3 GeV, the values of Z_{pp} generated by PYTHIA [39] slightly

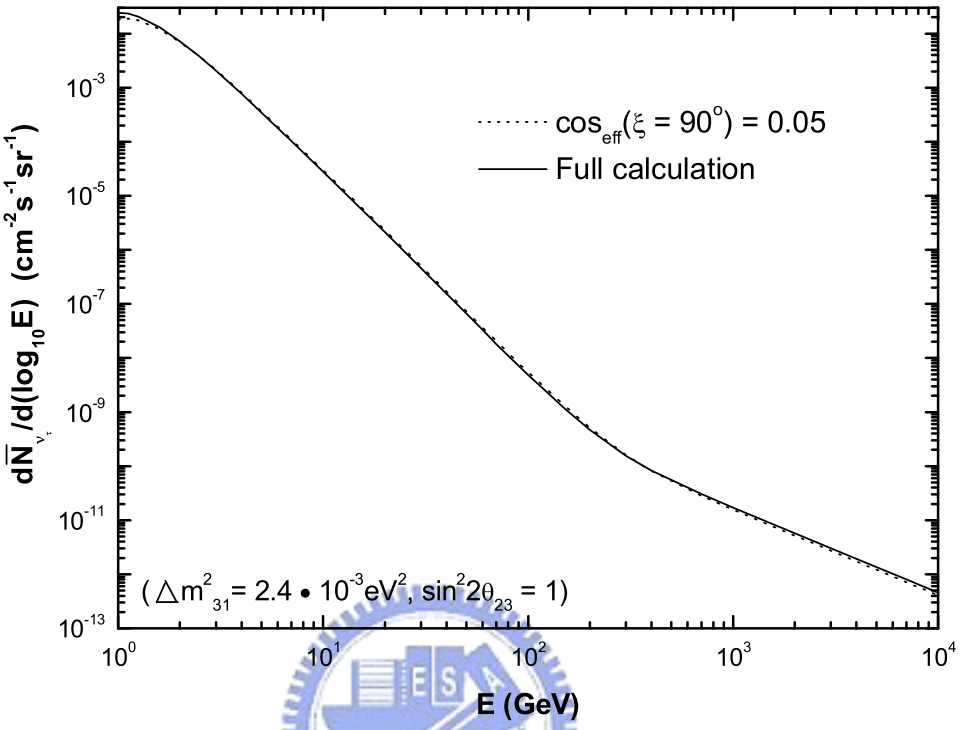

Figure 3.8: The comparison of atmospheric ν_τ flux obtained by using $\cos_{\rm eff}\xi$ and that obtained by the full calculation for $\xi = 90°$.

depend on the energy and roughly twice larger than the value we have so far used for calculations. We check the effect of Z_{pp} by calculating the atmospheric ν_τ flux with the PYTHIA-generated Z_{pp}. The comparison of this result with the earlier one obtained by setting $Z_{pp} = 0.263$ is shown in Fig. 3.9 for $\xi = 0°$ and Fig. 3.10 for $\xi = 90°$. For the $\xi = 0°$ case, two set of results do not exhibit noticeable difference until $E_\nu \geq 10$ GeV. At $E_\nu = 100$ GeV, they differ by 45%. At $E_\nu = 1$ GeV, two results differ by 46% while they differ by 29% at $E_\nu = 100$ GeV. Obviously, the behavior of Z_{pp} is one of the major uncertainties for determining the atmospheric ν_τ flux.

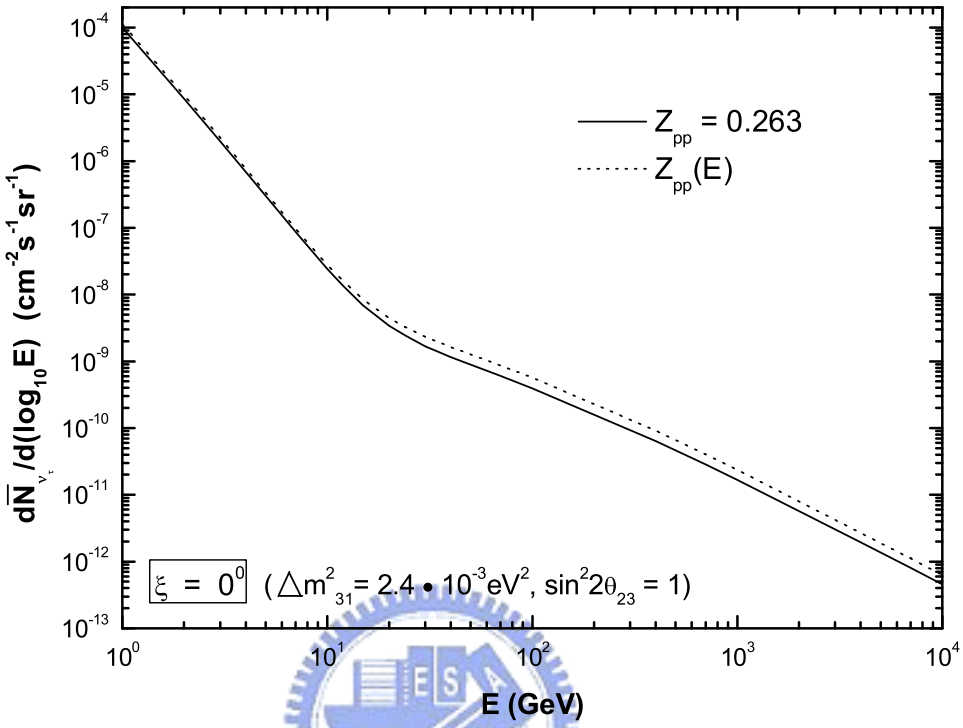

Figure 3.9: The comparison of atmospheric ν_τ fluxes calculated from a constant Z_{pp} [41, 42] and an energy-dependent Z_{pp} [44] for $\xi = 0°$.

B. Muon-Decay contributions

As mentioned earlier, the muon-decay contributions to ν_μ is non-negligible for neutrino energies less than 10 GeV. Such ν_μ's can oscillate into ν_τ's during their propagations in the atmosphere. The calculation of such a flux according to Eqs. (3.12) and (3.17) is rather involved. However, a simple approximation as presented below gives a rather accurate result for this flux.

To calculate ν_μ spectrum due to muon decays, we require the knowledge of muon polarizations. The muon polarization however depends on the ratio of muon momentum to the momentum of parent pion or kaon as indicated by

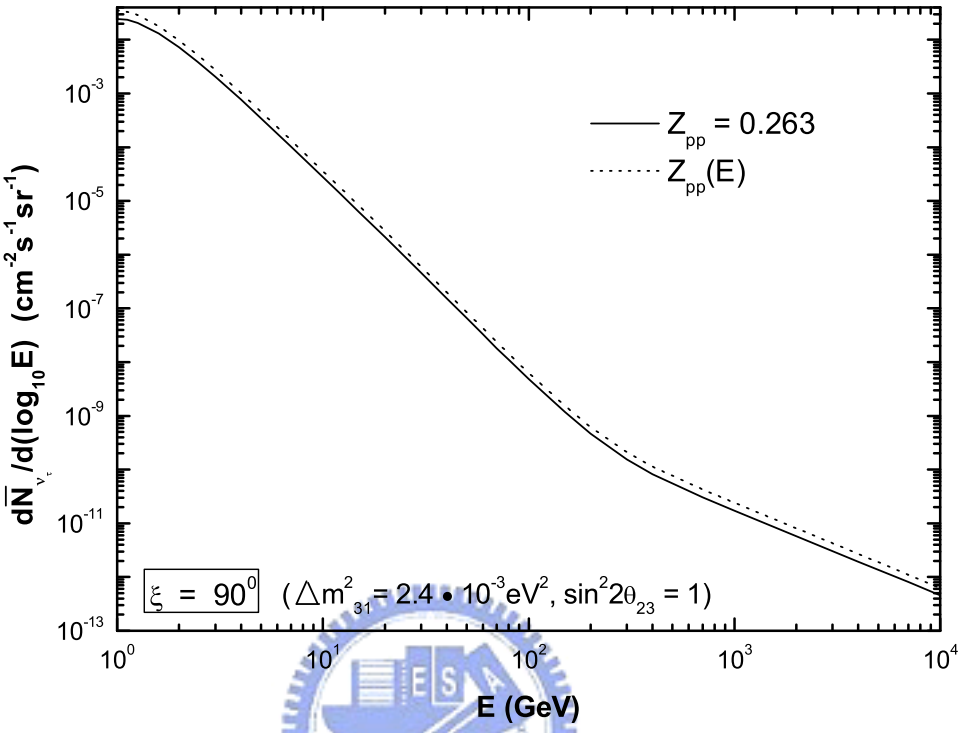

Figure 3.10: The comparison of atmospheric ν_τ fluxes calculated from a constant Z_{pp} [41, 42] and an energy-dependent Z_{pp} [44] for $\xi = 90°$.

Eq. (3.16). It is straightforward to calculate the average muon polarization at any slant depth X provided the energy spectrum of the parent pion or kaon is known at that point. For the downward case ($\xi = 0°$), it is known from the previous section that the muons are most likely produced at around 14 km from the ground detector. At that point, the pion and kaon fluxes can be approximately parameterized as $\phi_\pi(E_\pi) = 10^{-3.15} \cdot E_\pi^{-2.02}$ and $\phi_K(E_K) = 10^{-5.11} \cdot E_K^{-1.74}$ in units of $\mathrm{cm}^{-2}\mathrm{s}^{-1}\mathrm{sr}^{-1}\mathrm{GeV}^{-1}$ for meson energies between 1 and few tens of GeV. We do not distinguish $\pi^-(K^-)$ from $\pi^+(K^+)$ in the above fittings. Although the spectra are charge dependent, the resulting absolute values of μ^+ polarization and μ^- polarization differ by only 10% for E_μ up to

few tens of GeV [42]. From Eq. (3.16), and the above pion and kaon spectra, we obtain $\langle P^{\pi}_{\mu^-} \rangle = 0.35$, $\langle P^{K}_{\mu^-} \rangle = 0.95$. Therefore μ^- coming from the π^- decays are 67% right-handed polarized and 33% left-handed polarized. On the other hand, μ^- coming from K^- decays are 98% right-handed polarized and only 2% left-handed polarized. The muons produced by meson decays lose energies before they decay into neutrinos. The decay distribution for $\mu^- \to \nu_\mu$ is given by Eq. (3.18). The average momentum fraction $\langle y \rangle$ of muon neutrinos are 0.3 and 0.4 from decays of right-handed and left-handed μ^-. Following a similar procedure, one can determine the polarization and decay distributions of μ^+. Finally, to calculate the spectrum of muon neutrinos arising from muon decays, we use the approximation of replacing $F_{\mu^{\pm}_s \to \nu_\mu}(E/E_\mu)$ with $\delta(E/E_\mu - \langle y \rangle)$ in Eq. (3.17).

For checking the validity of the above approximation, we compare our result on the fraction of muon decay contribution to the overall ν_μ flux with that given by Ref. [42] for $\cos\xi = 0.4$, i.e., $\xi = 66°$. At this zenith angle, most of the muons are produced roughly 45 km from the detector. The pion and kaon fluxes at this point are fitted to be $\phi_\pi(E_\pi) = 10^{-3.65} \cdot E_\pi^{-1.88}$ and $\phi_K(E_K) = 10^{-5.57} \cdot E_K^{-1.69}$ in units of $\mathrm{cm}^{-2}\mathrm{s}^{-1}\mathrm{sr}^{-1}\mathrm{GeV}^{-1}$. This gives rise to $\langle P^{\pi}_{\mu^-} \rangle = 0.34$, $\langle P^{K}_{\mu^-} \rangle = 0.94$. Following the procedure in the downward case, we obtain the muon neutrino flux from the muon decays. At $E_\nu = 1$ GeV, the fraction of muon-decay contributions to the overall ν_μ flux is 44% while the fraction decreases to 17% at $E_\nu = 10$ GeV. In Ref. [42], the corresponding fractions are 47% and 18% respectively. Both set of fractions agree rather well.

After confirming that our approximation works well for calculating the muon-decay contributions to the atmospheric ν_μ flux, we can proceed to calculate the resulting atmospheric ν_τ flux with Eq. (3.23). Specifically we only need to include the first term on the R.H.S. of Eq. (3.23) because the second term has already been included in the two-body decay contribution. In Fig. 3.11, those atmospheric ν_τ fluxes resulting from oscillations of ν_μ's out of both two- and

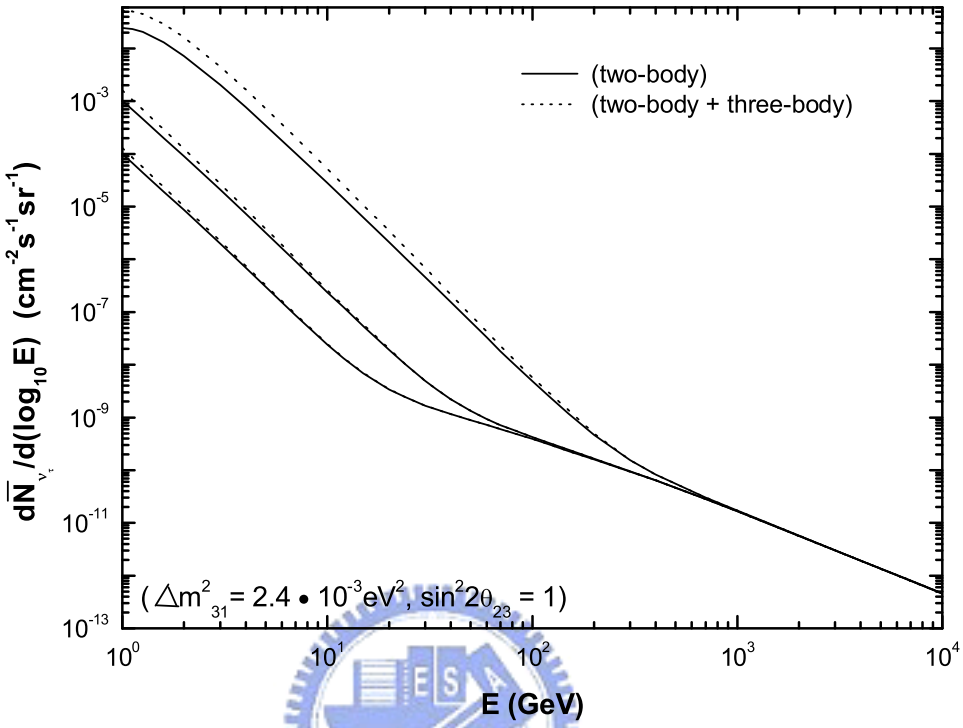

Figure 3.11: The comparisons of atmospheric ν_τ fluxes resulting from the oscillations of ν_μ's generated from two-body and three-body decays with those resulting from the oscillations of ν_μ's generated from two-body decays alone. The comparisons are made for three zenith angles, $\cos\xi = 0,\ 0.4$, and 1 (from top to bottom).

three-body decays (muon decays) are compared with those resulting from the oscillations of ν_μ's originated from two-body decays alone. As expected, the three-body decay contribution is non-negligible for $E_\nu \leq 10$ GeV. Quantitatively, for $\xi = 0°$ and $E_\nu = 1$ GeV, 24% of the total atmospheric ν_τ flux is from the oscillations of ν_μ's originated from the muon decays. At $E_\nu = 10$ GeV, only 2.9% of the total atmospheric ν_τ flux comes from the same source. For $\xi = 66°$, the three-body decay contribution gives rise to 36% and 8.9% of the total atmospheric ν_τ flux at $E_\nu = 1$ GeV and $E_\nu = 10$ GeV respectively. Finally, for

$\xi = 90°$, the three-body decay contribution to the total atmospheric ν_τ flux is most significant. It contributes to 53%, 46%, and 39% of the total atmospheric ν_τ flux at $E_\nu = 1$ GeV, 10 GeV and 20 GeV respectively. To calculate the three-body decay contribution to ν_μ flux at $\xi = 90°$, we have used Eq. (3.9) for the meson survival probability with $\cos_{\rm eff}\,\xi = 0.05$ and a overall factor $C \approx 1.40$ to fix the normalization of the flux [61].

3.3.2 The Upward Atmospheric Tau Neutrino Flux

The upward atmospheric ν_τ flux is enhanced compared to the downward case since the average neutrino path length increases. Therefore the observation of astrophysical tau neutrinos is subject to a more serious background problem in such a case. However, the observation of atmospheric tau neutrinos is also interesting in its own right. The atmospheric tau neutrino flux for $\cos\xi = -0.2$ is given in Fig. 3.12. The effect of $\nu_\mu \to \nu_\tau$ oscillation is evident for below TeV energies. This is seen from the slope change of the atmospheric ν_τ flux. The atmospheric ν_τ flux shows oscillatory behavior for $E \leq 10$ GeV. For $\cos\xi < -0.2$, such an oscillatory behavior is even more significant. In such a case, it is more practical to study the averaged flux. We average the atmospheric ν_τ flux for the zenith angle range $-1 \leq \cos\xi \leq -0.4$, as shown in Fig. 3.13. Due to uncertainties of the intrinsic atmospheric ν_τ flux, the atmospheric ν_τ flux taking into account the oscillation effect also contains uncertainties beginning at a few hundred GeV's. In the same figure, we also plot the corresponding atmospheric ν_μ flux. The ν_μ and ν_τ fluxes are comparable for $E < 30$ GeV. In such a case, the footprint of ν_τ might be identified by studying the energy spectra of shower events induced by neutrino interactions [62]. At $E = 10^4$ GeV, the ν_μ flux is approximately 30 times larger than the maximal ν_τ flux. We note that the maximal and minimal ν_τ fluxes begin to differ at $E = 500$ GeV. At $E = 1$ TeV, the maximal flux is 3 times larger than the minimal one. The ratio of maximal flux to the minimal one increases to 14 at $E = 10$ TeV. We

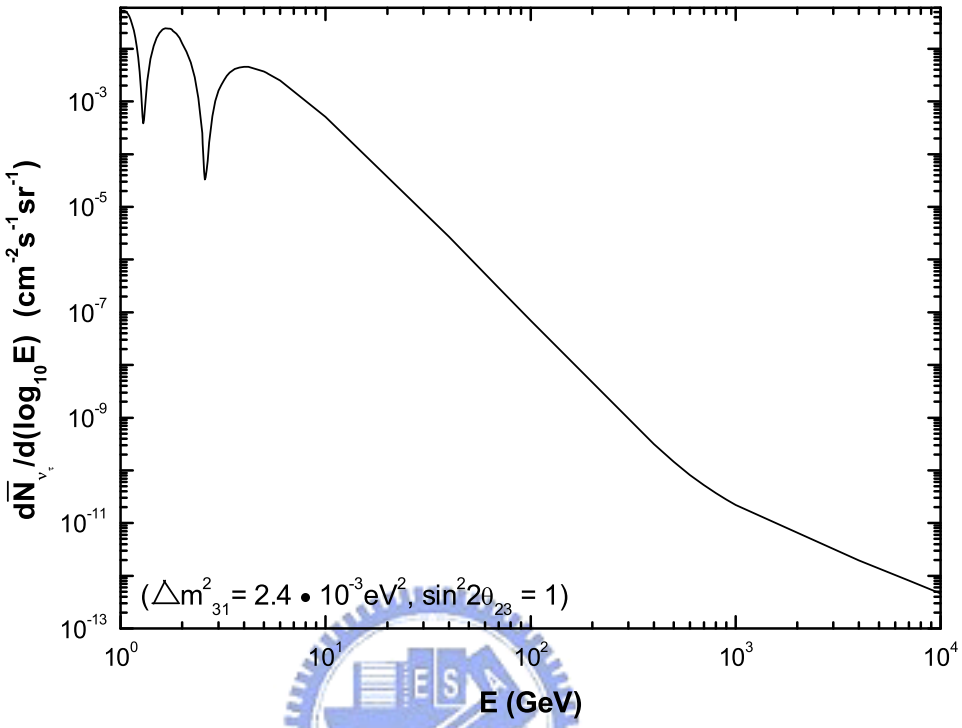

Figure 3.12: The atmospheric ν_τ flux for $\cos\xi = -0.2$ with $\sin^2 2\theta_{23} = 1$, $\Delta m^2_{31} = 2.4 \cdot 10^{-3}$ eV^2, and $Z_{pp} = 0.263$.

remark that the upward atmospheric ν_τ flux is also calculated in Ref. [62] with $\Delta m^2_{31} = 10^{-2}$, $10^{-2.5}$, 10^{-3} eV^2 respectively. Here we have done the calculation with the best fit value of Δm^2_{31} taken from [32]. Furthermore we include the contribution of intrinsic atmospheric ν_τ flux and its associated uncertainties.

3.3.3 Comparison and Discussion

The comparison of the galactic-plane and the downward going atmospheric ν_τ flux is given in Fig. 3.14. The former flux clearly `dominates` the latter for $E \geq 10$ GeV, whereas the two fluxes cross at $E = 2.3$ GeV for $\Delta m^2_{31} = 2.4 \cdot 10^{-3}$ eV^2 and $\sin^2 2\theta_{23} = 1$. This comparison is however subject to the

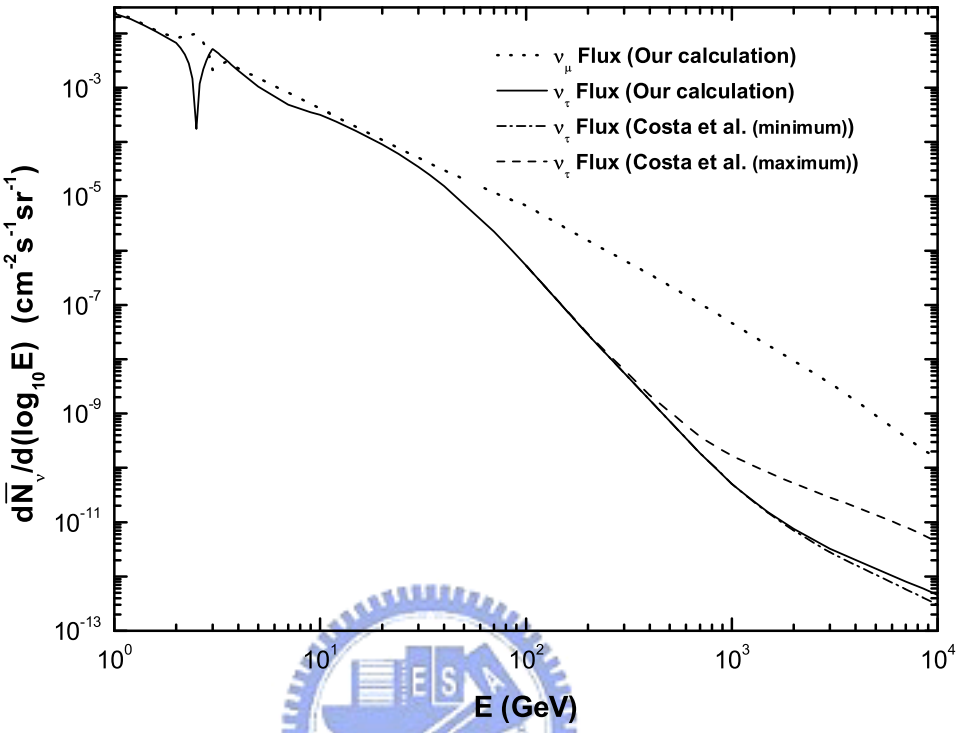

Figure 3.13: The atmospheric ν_τ flux averaged for $-1 \leq \cos\xi \leq -0.4$. The uncertainty of this flux due to the uncertainty of intrinsic atmospheric ν_τ flux is also shown. We take the maximum and minimum intrinsic atmospheric ν_τ fluxes given in [58] to calculate the total atmospheric ν_τ fluxes on the Earth.

uncertainty of galactic-plane ν_τ flux by the choices of the density n_p and the distance R mentioned before. One can see that the atmospheric ν_τ flux is sensitive to the value of Δm^2_{31} for $E \leq 20$ GeV. Furthermore, a change of slope occurs for the atmospheric ν_τ flux at $E \approx 20$ GeV. Beyond this energy, the slope of the atmospheric ν_τ flux is identical to that of the galactic-plane ν_τ flux. `For` $E > 20$ `GeV, the atmospheric` ν_τ `flux is intrinsic`, i.e., coming from the D_s decays, whereas the galactic-plane ν_τ flux arises from the oscillation of the ν_μ, which is produced mainly by the π decays. In both cases,

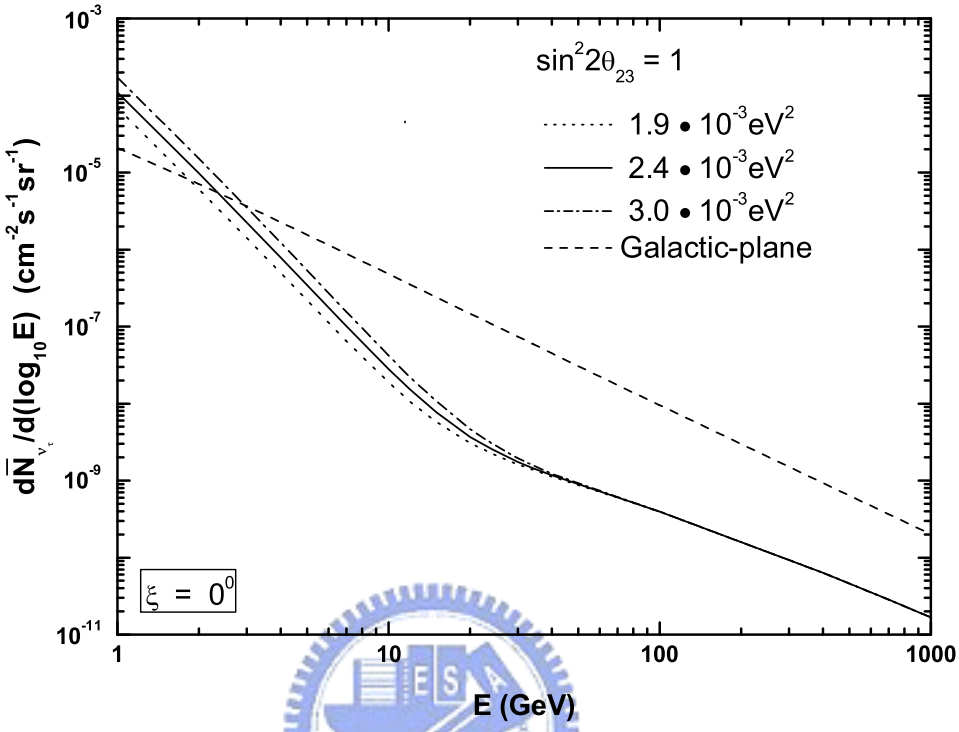

Figure 3.14: The comparison of the galactic-plane and the downward going atmospheric ν_τ fluxes in the presence of neutrino oscillations with maximal mixing as a function of the neutrino energy in GeV. We have included downward going atmospheric ν_τ fluxes for $\Delta m^2_{31} = 1.9 \cdot 10^{-3}$ eV^2, $2.4 \cdot 10^{-3}$ eV^2 and $3 \cdot 10^{-3}$ eV^2 (from bottom to top).

the hadrons decay before interacting with the medium. Such a feature dictates the slope of the outgoing neutrino flux. Below 20 GeV, however, the atmospheric ν_τ flux predominantly comes from the ν_μ oscillations, i.e., $\phi^{\rm tot}_{\nu_\tau}(E) \approx \phi_{\nu_\mu}(E) \cdot \sin^2 2\theta_{23} \cdot \sin^2(L/L_{\rm osc})$ following Eq. (3.2). Since $L_{\rm osc} \equiv 4E/\Delta m^2_{31} \approx 330$ km for $E = 1$ GeV with $\Delta m^2_{31} = 2.4 \cdot 10^{-3}$ eV^2, we approximate $\sin^2(L/L_{\rm osc})$ with $(L/L_{\rm osc})^2$ so that $\phi^{\rm tot}_{\nu_\tau}(E) \sim \phi_{\nu_\mu}(E) E^{-2}$. Because the neutrino oscillation effect steepens the ϕ_{ν_τ} spectrum for $E \leq 20$ GeV, the slope change of ϕ_{ν_τ} at $E \approx 20$ GeV is significant. Furthermore, for $E \leq 20$ GeV, the galactic-plane

tau neutrino flux has a rather different slope from that of the atmospheric ν_τ flux. This is an important criterion for distinguishing the two fluxes, particu-

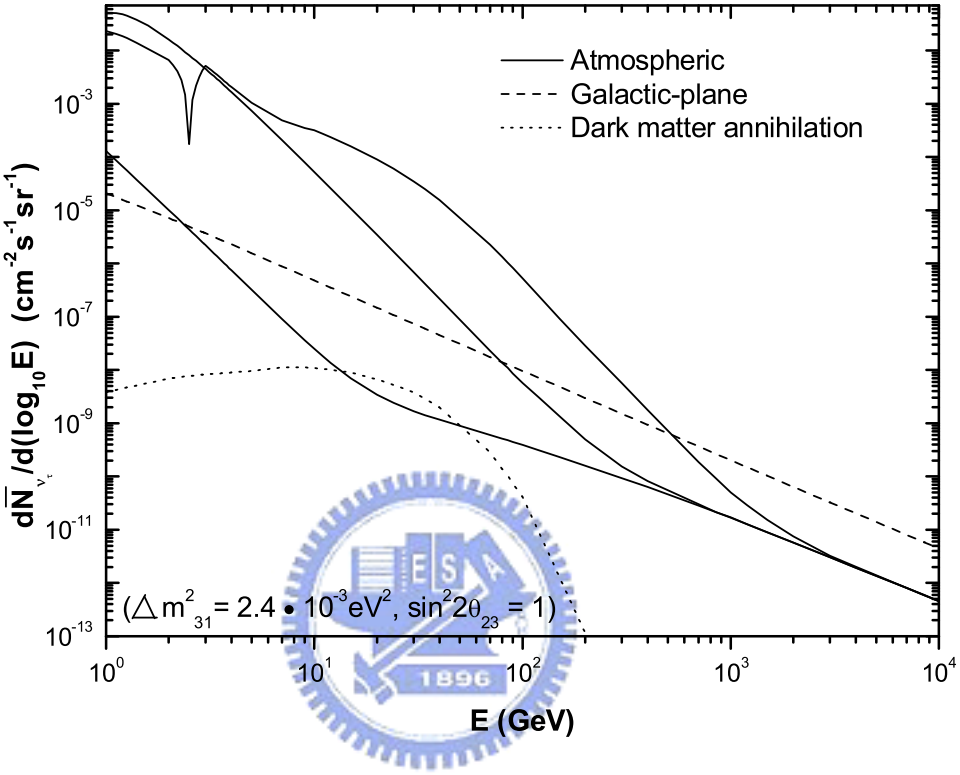

Figure 3.15: The comparison of atmospheric ν_τ fluxes with the galactic-plane tau neutrino flux [52] and the tau neutrino flux due to the neutralino dark matter annihilations [63]. We have included downward ($\cos\xi = 1$), horizontal ($\cos\xi = 0$) and upward ($-1 \leq \cos\xi \leq -0.4$) atmospheric ν_τ fluxes for the comparison. Among them, the downward flux is the smallest while the upward flux has a dip near $E = 2.5$ GeV.

larly given that the normalization of the galactic-plane tau neutrino flux is still uncertain.

Since we have obtained a complete result of the atmospheric ν_τ flux for the entire zenith angle range, we compare this flux with the galactic-plane tau neutrino flux just mentioned and the cosmological ν_τ flux due to neutralino

dark matter annihilations [63]. The comparison is depicted in Fig. 3.15. One can see that the galactic-plane ν_τ flux dominates over the downward ($\xi = 0°$) atmospheric ν_τ flux for E_ν greater than a few GeV. Hence, in this direction, it is possible to observe the flux of galactic-plane tau neutrinos in the GeV energy range. For near horizontal directions, the atmospheric ν_τ flux grows rapidly with zenith angles. Therefore, for $\xi = 90°$, the energy threshold for galactic-plane tau neutrino flux to dominate over its atmospheric counterpart is pushed up to $E_\nu > 100$ GeV. We further see that the galactic-plane ν_τ flux does not dominate the upward atmospheric ν_τ background ($-1 \leq \cos\xi \leq -0.4$) until $E = 500$ GeV. On the other hand, the comparison of the upward atmospheric ν_τ flux with the horizontal one is also interesting. Two fluxes are in fact comparable for $E < 10$ GeV. This shows that the $\nu_\mu \rightarrow \nu_\tau$ oscillation is already quite significant in the horizontal direction for such an energy range. Nevertheless, the upward atmospheric ν_τ flux takes over from $E_\nu \geq 10$ GeV until $E \approx 2$ TeV where two fluxes merge again. From Fig. 3.15, it is also clear that the atmospheric ν_τ flux is a non-negligible background to the cosmological tau neutrino flux due to neutralino dark matter annihilations [63]. In fact, two fluxes are comparable in the downward direction while the atmospheric ν_τ flux is significantly larger in horizontal and upward directions.

The results presented in Figs. 3.14 and 3.15 indicate the opportunities for the tau neutrino astronomy in the GeV energies for the incident zenith angles $0° \leq \xi \leq 180°$ in the two neutrino flavor mixing approximation. We point out that the dominance of the galactic-plane tau neutrino flux over its atmospheric background in GeV energies is `unique` among all the considered neutrino flavors. This is depicted in Fig. 3.16. Because of the $\nu_\mu \rightarrow \nu_\tau$ neutrino oscillations, the `total` galactic ν_τ flux is identical to that of the galactic ν_μ flux. However, the atmospheric ν_μ flux is much larger than the atmospheric ν_τ flux. As a result, in the `presence` of neutrino oscillations, the crossing energy value for the galactic-plane and the atmospheric ν_μ fluxes is pushed up to $5 \cdot 10^5$ GeV,

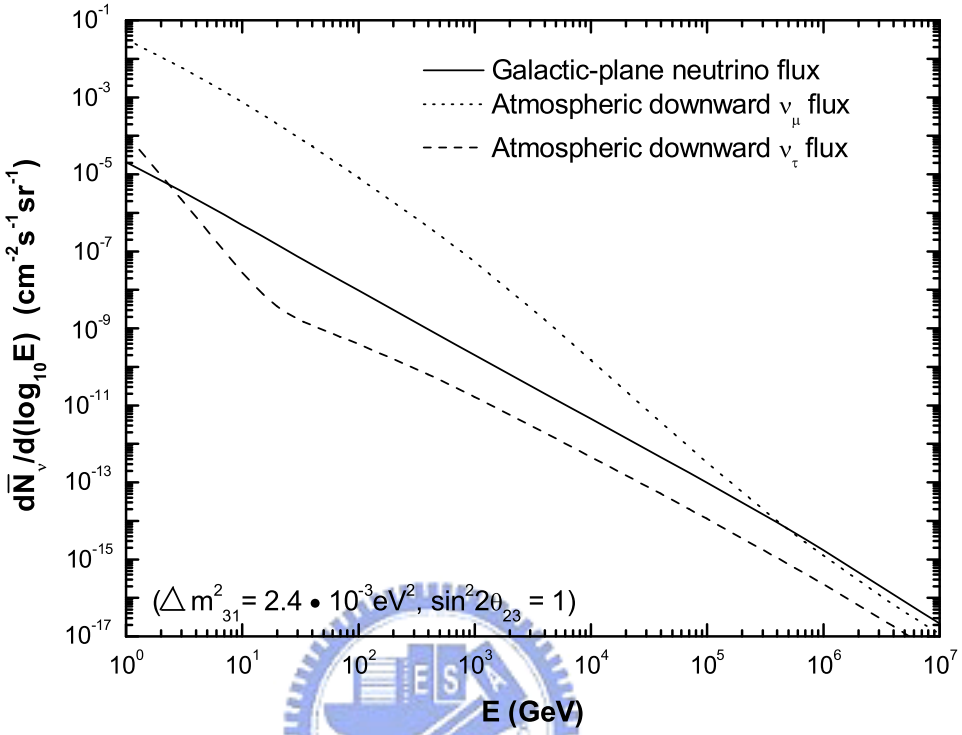

Figure 3.16: An illustrative comparison of the downward going atmospheric ν_μ and ν_τ fluxes and the corresponding galactic-plane neutrino fluxes in the presence of neutrino oscillations as a function of the neutrino energy in GeV. The galactic-plane and the atmospheric ν_μ fluxes cross at $E = 5 \cdot 10^5$ GeV.

which is drastically different from the tau neutrino case.

3.4 The Atmospheric Tau Neutrino Flux With Oscillations In The Three-Flavor Mixing Scheme

In this section, we study the atmospheric tau neutrino flux with oscillations in the three-flavor mixing scheme. We first calculate the intrinsic atmospheric ν_e flux. Since the atmospheric ν_e results from the three-body muon decays, the ν_e

flux is given by [42]

$$\frac{\mathrm{d}^2 N_{\nu_e}^{\mu^\pm}(E,\xi,X)}{\mathrm{d}E\mathrm{d}X} = \sum_{s=L,R}\int_E^\infty \mathrm{d}E_\mu \frac{F_{\mu_s^\pm\to\nu_e}(E/E_\mu)}{d_\mu(E_\mu,X)E_\mu}\cdot\frac{\mathrm{d}N_{\mu_s^\pm}(E_\mu,\xi,X)}{\mathrm{d}E_\mu}, \tag{3.24}$$

where $d_\mu(E_\mu,X)$ is the muon decay length in units of g/cm^2 at the slant depth X and $F_{\mu_s^\pm\to\nu_e}(E/E_\mu)$ is the decay distribution of $\mu_s^\pm\to\nu_e$. Precisely, in the ultra-relativistic limit, one has [42]

$$F_{\mu^-\to\nu_e}(y) = g_0(y) + P_\mu g_1(y), \tag{3.25}$$

with $g_0(y) = 2-6y^2+4y^3$ and $g_1(y) = -2+12y-18y^2+8y^3$. The average momentum fraction $\langle y\rangle$ of electron neutrinos are 0.4 and 0.2 from decays of right-handed and left-handed μ^- respectively. We use the approximation of replacing $F_{\mu_s^\pm\to\nu_e}(E/E_\mu)$ with $\delta(E/E_\mu-\langle y\rangle)$ in Eq. (3.24) to calculate the spectrum of electron neutrinos arising from muon decays.

Having obtained the intrinsic atmospheric ν_e flux, the atmospheric tau neutrino flux with oscillations in the three-flavor mixing scheme can be calculated using

$$\begin{aligned}\frac{\mathrm{d}\bar{N}_{\nu_\tau}(E,\xi)}{\mathrm{d}E} &= \int_0^{X_{\max}(\xi)}\mathrm{d}X\left[\frac{\mathrm{d}^2 N_{\nu_\mu}(E,\xi,X)}{\mathrm{d}E\mathrm{d}X}\cdot P_{\nu_\mu\to\nu_\tau}\left(E,L(X,\xi)\right)\right.\\ &\quad+\frac{\mathrm{d}^2 N_{\nu_e}(E,\xi,X)}{\mathrm{d}E\mathrm{d}X}\cdot P_{\nu_e\to\nu_\tau}\left(E,L(X,\xi)\right)\\ &\quad\left.+\frac{\mathrm{d}^2 N_{\nu_\tau}(E,\xi,X)}{\mathrm{d}E\mathrm{d}X}\cdot\left(1-P_{\nu_\mu\to\nu_\tau}-P_{\nu_e\to\nu_\tau}\right)\right],\end{aligned} \tag{3.26}$$

where $P_{\nu_\mu\to\nu_\tau}\left(E,L(X,\xi)\right)$ and $P_{\nu_e\to\nu_\tau}\left(E,L(X,\xi)\right)$ are the $\nu_\mu\to\nu_\tau$ and $\nu_e\to\nu_\tau$ oscillation probability in the three-flavor mixing scheme (see Appendix B) [43], assuming a non-vanishing θ_{13}. We note that the matter effect has been taken into account in deriving $P_{\nu_\mu\to\nu_\tau}$ and $P_{\nu_e\to\nu_\tau}$. We use the Stacey model [64] for the Earth density profile. In the Stacey model, the mean matter densities in the Earth core and in the Earth mantle are: $\rho_c\cong 12$ g/cm^3 and $\rho_m\cong 5$ g/cm^3 respectively. We calculate the upward (averaged for $-1\le\cos\xi\le-0.4$) atmospheric ν_τ fluxes with $\sin^2 2\theta_{13}=0.1$ and 0.05 respectively while maintaining

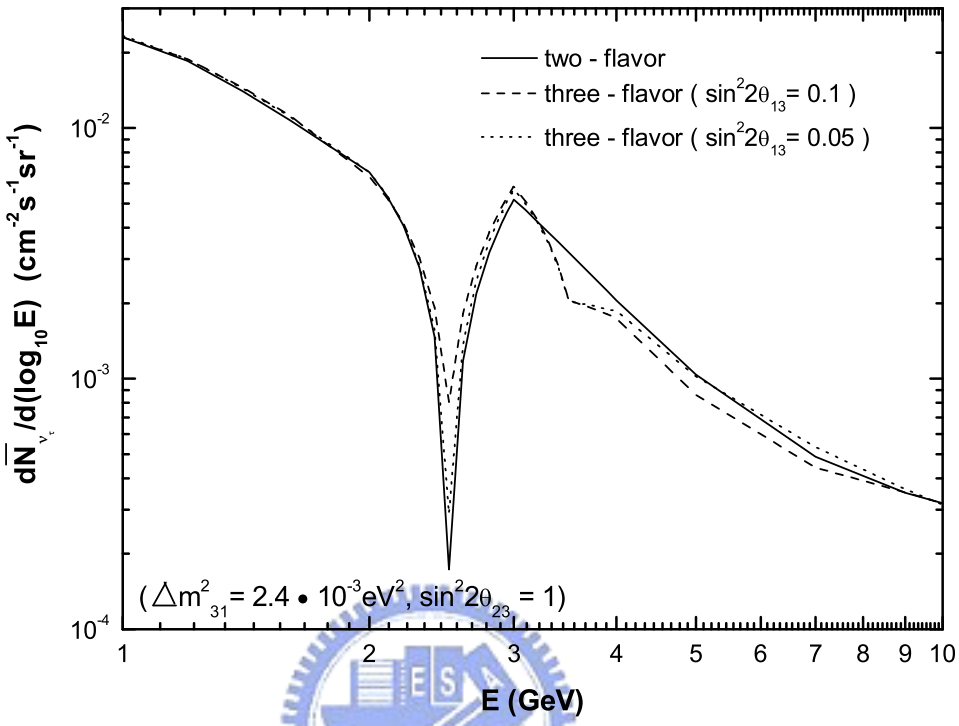

Figure 3.17: The comparison of atmospheric ν_τ flux in the three-flavor mixing scheme with that in the two-flavor mixing scheme. In the former case, we include atmospheric ν_τ fluxes for $\sin^2 2\theta_{13} = 0.1$ and 0.05 respectively.

$\sin^2 2\theta_{23} = 1$ and $\Delta m^2_{31} = 2.4 \cdot 10^{-3}$ eV^2. We compare these two fluxes with the upward atmospheric ν_τ flux obtained by the two-flavor mixing scheme. The comparison is depicted in Fig. 3.17. For $1 \leq E_\nu/\text{GeV} \leq 10$, one can see that these three curves behave similarly. At the vicinity of $E_\nu = 2.5$ GeV, all three fluxes reach their local minima and the ratio of them is $1 : 4.7 : 1.7$. On the other hand, at the vicinity of $E_\nu = 3$ GeV, three fluxes reach their local maxima and the ratio of them is $1 : 1.13 : 1.1$. For $E_\nu \geq 10$ GeV, three fluxes merge.

Following the same approach, we can also calculate the upward atmospheric ν_μ and ν_e fluxes in the three-flavor mixing scheme. The comparison of at-

mospheric ν_μ flux in the three-flavor mixing scheme with that in the two-flavor mixing scheme is depicted in Fig. 3.18. At the vicinity of $E_\nu = 2.5$ GeV, all three fluxes reach their local maxima and the ratio of them is 1.12 : 1 : 1.07 . on the other hand, at the vicinity of $E_\nu = 3$ GeV, all three fluxes reach their local minima and the ratio of them is 1.86 : 1 : 1.02 . Finally, the comparison of

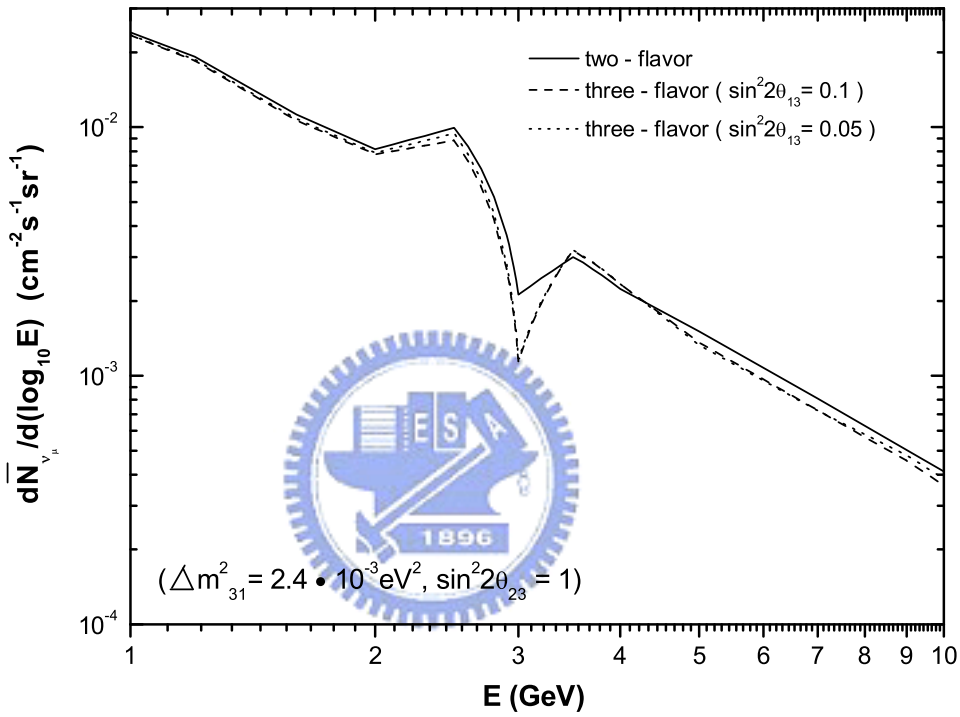

Figure 3.18: The comparison of atmospheric ν_μ flux in the three-flavor mixing scheme with that in the two-flavor mixing scheme. In the former case, we include atmospheric ν_τ fluxes for $\sin^2 2\theta_{13} = 0.1$ and 0.05 respectively.

atmospheric ν_e flux in the three-flavor mixing scheme with that in the two-flavor mixing scheme is depicted in Fig. 3.19. We note that these three fluxes differ significantly around $E_\nu = 7$ GeV and the ratio of them at $E_\nu = 7$ GeV is 1 : 2.28 : 1.88 . They merge for $E_\nu \geq 20$ GeV.

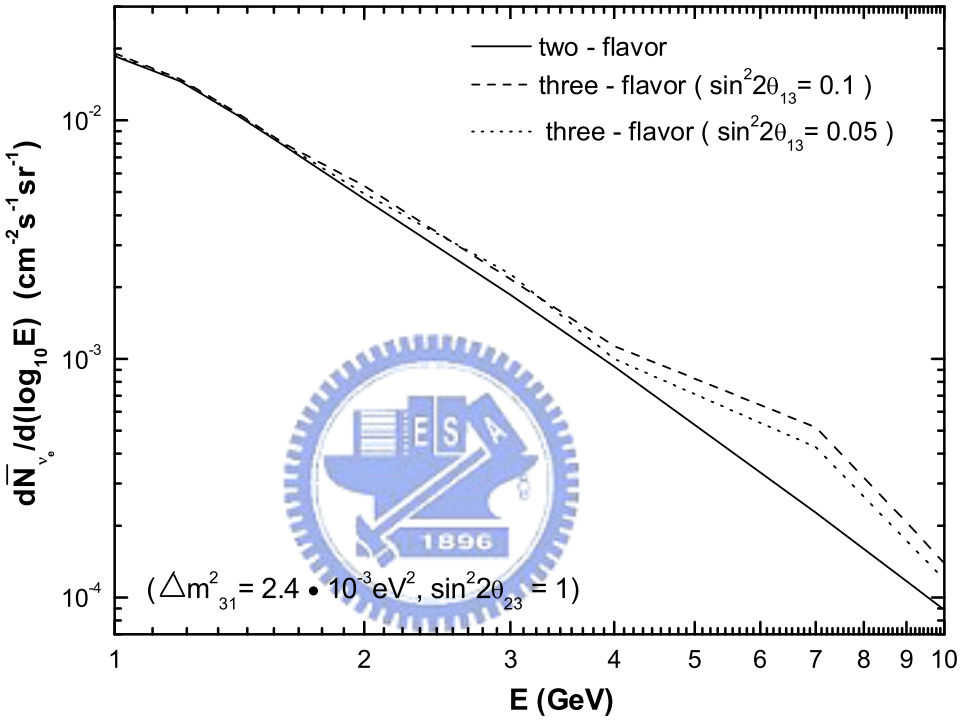

Figure 3.19: The comparison of atmospheric ν_e flux in the three-flavor mixing scheme with that in the two-flavor mixing scheme. In the former case, we include atmospheric ν_τ fluxes for $\sin^2 2\theta_{13} = 0.1$ and 0.05 respectively.

Chapter 4

Conclusions

To summarize the work in this thesis, first, in Chap. 2, we have given a semi-analytic treatment on the problem of simultaneous propagation of high energy tau neutrinos and tau leptons inside the Earth. Our treatment explicitly takes into account the `inelasticity` of neutrino-nucleon scatterings as well as the tau-lepton `energy loss`. We specifically considered the Earth-skimming situation and provided detailed results for the energy dependencies of emerging tau-lepton fluxes resulting from a few anticipated astrophysical neutrino fluxes. The effect of matter density on the tau-lepton flux is also studied. Such an effect is found to be related to the spectrum index of incident neutrino flux. Our treatment thus provides a basis for a more complete and realistic assessment of high-energy-neutrino flux measurements in the under-construction/planning large neutrino telescopes.

Secondly, in Chap. 3, we have performed a detailed calculation of atmospheric ν_τ flux for zenith angles $0 \leq \xi \leq 180^\circ$ in Chap. 3. In this chapter, a comparison of the galactic-plane ν_τ flux with the atmospheric ν_τ flux is made for illustrating the possibility of the tau neutrino astronomy. We also compare the atmospheric ν_τ flux with the cosmological ν_τ flux due to neutralino dark matter annihilations [63]. From Fig. 3.15, we note that the galactic-plane ν_τ flux dominates over the downward ($\xi = 0^\circ$) atmospheric ν_τ flux for E_ν greater than a few GeV

and therefore it is possible to observe the flux of galactic-plane tau neutrinos in the GeV energy range along the downward direction. For near horizontal directions, the atmospheric ν_τ flux grows rapidly with zenith angles. Hence, for $\xi = 90°$, the energy threshold for galactic-plane tau neutrino flux to dominate over its atmospheric counterpart is pushed up to $E_\nu > 100$ GeV. Furthermore, one can see that the galactic-plane ν_τ flux does not dominate the upward atmospheric ν_τ background ($-1 \leq \cos\xi \leq -0.4$) until $E = 500$ GeV. However, it is noteworthy that, in the muon neutrino case, galactic-plane neutrino flux is overwhelmed by the atmospheric background until $E_\nu > 10^6$ GeV [65]. Such a difference between ν_μ and ν_τ shows the promise of the tau neutrino astronomy in the GeV energy range [35, 52]. On the other hand, we can also see from Fig. 3.15 that the atmospheric ν_τ flux is a non-negligible background to the cosmological tau neutrino flux due to neutralino dark matter annihilations [63]. In the last section of this chapter, we take into account the matter effects to neutrino oscillations and calculate the atmospheric tau neutrino flux with oscillations in the three-flavor mixing scheme. To sum up the work in Chap. 3, we have presented a semi-analytical calculation on the atmospheric ν_τ flux due to $\nu_\mu \to \nu_\tau$ oscillations for downward, upward, and horizontal directions. The atmospheric ν_τ flux at $\xi = 90°$ is two orders of magnitude larger than the corresponding flux at $\xi = 0°$ for $1 \leq E_\nu/\text{GeV} \leq 10$ while fluxes with zenith angles between 0 and 90 degrees merge for $E_\nu \geq 700$ GeV. The upward atmospheric ν_τ fluxes show oscillatory behaviors. For the averaged flux with $-1 \leq \cos\xi \leq -0.4$, the atmospheric ν_τ flux is found to be comparable to the atmospheric ν_μ flux for $E < 30$ GeV. Concerning the uncertainties in our calculations, we have studied the dependencies of atmospheric ν_τ flux on the Z moment Z_{pp} for representative zenith angles $\xi = 0°$ and $\xi = 90°$. We have also discussed in detail the uncertainty of intrinsic atmospheric ν_τ flux due to different models for charm hadron productions. The consequence of such a uncertainty on the determination of oscillated ν_τ flux is studied as well. Concerning the technique for calculating

the atmospheric ν_τ flux from large zenith angles, we have verified the validity of using $\cos_{\rm eff}\xi$ in Eq. (3.9) to calculate the atmospheric ν_τ flux for $\xi > 60^\circ$. In particular, we have extrapolated the results in Ref. [61] to $\xi = 90^\circ$ and demonstrate that the choice $\cos_{\rm eff}(\xi = 90^\circ) = 0.05$ reproduces well the atmospheric ν_τ flux obtained by a full calculation using Eq. (3.8).

Finally, we note that there are possible backgrounds induced by the electron neutrino events and the neutral current events to the prospective observation of tau neutrino events . For $E < 10^3$ GeV, the tau lepton decay length is less than a mm. This tau lepton is produced in the detector in the galactic-plane tau neutrino induced interactions. There are certain specific signatures of the tau neutrino induced tau leptons such as the appearance of the kink at the tau lepton decay (absent for the electrons) [66], as well as the relative characteristic fractional energy sharing from the incident neutrino [62]. Thus we will require a large scale finely grained detector with a resolution of a few μm to disentangle the galactic-plane tau neutrino induced events from the events induced by the electron neutrinos and the neutral current events on the event-by-event basis.

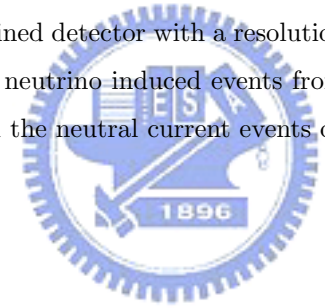

Appendix A

The iteration method for obtaining the $Z_\nu(E,X)$ and the $F_\tau(E,X)$

The evolution for F_{ν_τ} is given by Eq. (2.1). With the ansatz

$$F_{\nu_\tau}(E,X) = F_{\nu_\tau}(E,0)\exp\left(-\frac{X}{\Lambda_\nu(E,X)}\right), \tag{A.1}$$

we obtain the following equation for $Z_\nu(E,X)$:

$$\begin{aligned} XZ_\nu(E,X) &= \int_0^X \mathrm{d}X' \int_0^1 \frac{\mathrm{d}y}{1-y} \left\{ \frac{F^{(0)}_{\nu_\tau}(E_y)}{F^{(0)}_{\nu_\tau}(E)} \exp\left[-X' D_\nu(E,E_y,X')\right] \Phi^{\mathrm{NC}}_{\nu_\tau}(y,E) \right. \\ &+ \frac{F_\tau(E_y,X')}{F^{(0)}_{\nu_\tau}(E)} \left(\frac{\lambda_\nu(E)}{\rho d_\tau(E)}\right) \exp\left(\frac{X'}{\Lambda_\nu(E,X')}\right) \Phi^d_\tau(y,E) \\ &+ \left. \frac{F_\tau(E_y,X')}{F^{(0)}_{\nu_\tau}(E)} \left(\frac{\lambda_\nu(E)}{\lambda_\tau(E)}\right) \exp\left(\frac{X'}{\Lambda_\nu(E,X')}\right) \Phi^{\mathrm{CC}}_\tau(y,E) \right\}, \end{aligned} \tag{A.2}$$

where $F^{(0)}_{\nu_\tau}(E) \equiv F_{\nu_\tau}(E,0)$, while $\Phi^{\mathrm{NC}}_{\nu_\tau}$, Φ^{CC}_τ and Φ^d_τ are respectively given by

$$\Phi^{\mathrm{NC}}_{\nu_\tau}(y,E) = \frac{\sum_T n_T \frac{\mathrm{d}\sigma_{\nu_\tau T\to\nu_\tau Y}}{\mathrm{d}y}(y,E_y)}{\sum_T n_T \sigma^{\mathrm{tot}}_{\nu_\tau T}(E)}, \tag{A.3}$$

$$\Phi^{\mathrm{CC}}_\tau(y,E) = \frac{\sum_T n_T \frac{\mathrm{d}\sigma_{\tau T\to\nu_\tau Y}}{\mathrm{d}y}(y,E_y)}{\sum_T n_T \sigma^{\mathrm{tot}}_{\tau T}(E)}, \tag{A.4}$$

$$\Phi_\tau^d(y,E) = \frac{1}{\Gamma_\tau(E)} \frac{\mathrm{d}\Gamma_{\tau\to\nu_\tau Y}}{\mathrm{d}y}(y,E_y), \tag{A.5}$$

with n_T the number of targets per unit mass of the medium, and

$$D_\nu(E,E_y,X) = \frac{1}{\Lambda_\nu(E_y,X)} - \frac{1}{\Lambda_\nu(E,X)}. \tag{A.6}$$

For the simplicity in notations, we take the lower and upper limits for the y integration to be 0 and 1 respectively. In reality, the limits depend on the actual kinematics of each process. One may impose these limits in the functions $\Phi_{\nu_\tau}^{\mathrm{NC}}$, Φ_τ^{CC} and Φ_τ^d.

To perform the iteration, we begin by setting $Z_{\nu(0)} = 0$. In this approximation, we have

$$F_{\nu_\tau(0)}(E,X) = F_{\nu_\tau}(E,0) \exp\left(-\frac{X}{\lambda_\nu(E,X)}\right). \tag{A.7}$$

Substituting $F_{\nu_\tau(0)}(E,X)$ into Eq. (2.8), we obtain the lowest order ν_τ flux, $F_{\tau(0)}(E,X)$. The first iteration for Z_ν, denoted by $Z_{\nu(1)}$ is calculable from Eq. (A.2) by substituting $F_{\nu_\tau(0)}(E,X)$, $F_{\tau(0)}(E,X)$, and $Z_{\nu(0)}$ into the R.H.S. of this equation. From $Z_{\nu(1)}$, we can then calculate $F_{\nu_\tau(1)}(E,X)$ and $F_{\tau(1)}(E,X)$, which corresponds to the results presented in this paper. We have checked the convergence of iteration procedure and have found negligible differences between $Z_{\nu(2)}$ and $Z_{\nu(1)}$ and their associated ν_τ and τ fluxes.

The value of Z_ν depends on the spectrum index of the neutrino flux, since it effectively gives the regeneration effect in the neutrino-nucleon scattering. In general, a flatter neutrino spectrum implies a larger Z_ν. The Z_ν is however not sensitive to the slant depth X. In the case of GRB neutrinos, where the flux decreases as E_ν^{-2} for $E_\nu < 10^7$ GeV, and decreases as E_ν^{-3} for energies greater than that, we obtain $Z_\nu^{\mathrm{GRB}} \approx 0.2$. For the AGN neutrino, Z_ν^{AGN} changes from 0.96 to 0.35 as E_ν runs from 10^5 GeV to 10^6 GeV. In this energy range, the neutrino flux decreases slower than $E_\nu^{-0.5}$. For E_ν greater than 10^8 GeV, Z_ν^{AGN} drops below 0.2 as the neutrino flux spectrum begins a steep fall. The values for Z_ν^{GZK} also follow the similar pattern.

Appendix B

The neutrino oscillation probabilities in the three-flavor mixing scheme

In this appendix, we list the oscillation probabilities for neutrino traversing the earth in the three-flavor mixing scheme. In the Stacey model, the incident neutrinos with the zenith angle $147^\circ \leq \xi \leq 180^\circ$ both traverse the Earth mantle and the Earth core. On the other hand, the incident neutrinos with the zenith angle $90^\circ \leq \xi \leq 147^\circ$ only traverse the Earth mantle. The oscillation probabilities for these two cases are as follows [43]:

1. For $90^\circ \leq \xi \leq 147^\circ$

$$\begin{aligned}
P_{\nu_\mu \to \nu_e} &= \sin^2 2\theta_{13}^m \sin^2 \theta_{23} \sin^2(1.27\Delta_{31}^m L/E), \\
P_{\nu_e \to \nu_\tau} &= \sin^2 2\theta_{13}^m \cos^2 \theta_{23} \sin^2(1.27\Delta_{31}^m L/E), \\
P_{\nu_\mu \to \nu_\tau} &= -\sin^2 2\theta_{13}^m \sin^2 \theta_{23} \cos\theta_{23} \sin^2(1.27\Delta_{31}^m L/E) \\
&+ \sin^2 \theta_{13}^m \sin^2 2\theta_{23} \sin^2(1.27(m_{31}^m)^2 L/E) \\
&+ \cos^2 \theta_{13}^m \sin^2 2\theta_{23} \sin^2(1.27(M_{31}^m)^2 L/E). \qquad \text{(B.1)}
\end{aligned}$$

where L is in km, E is in GeV and

$$\begin{aligned}
\Delta^m_{31} &= \sqrt{(\Delta m^2_{31}\sin 2\theta_{13})^2 + (A^m_e - \Delta m^2_{31}\cos 2\theta_{13})^2}, \\
(m^m_{31})^2 &= \frac{\Delta m^2_{31} + A^m_e - \Delta^m_{31}}{2}, \\
(M^m_{31})^2 &= \frac{\Delta m^2_{31} + A^m_e + \Delta^m_{31}}{2}, \\
\sin 2\theta^m_{13} &= \frac{\Delta m^2_{31}\sin 2\theta_{13}}{\Delta^m_{31}}.
\end{aligned} \tag{B.2}$$

with Δm^2_{31} the mass squared difference of the two neutrino mass eigenstates, θ_{23} and θ_{13} the mixing angles. Here, $A_e = 1.52 \times 10^{-4}$ eV^2 $Y_e\rho(\mathrm{g/cm^3})E(\mathrm{GeV})$ is the amplitude for $\nu_e e$ forward scattering in matter with Y_e denoting the electron fraction and ρ the matter density. Note that, since we set the CP violation phase δ to zero, we have

$$P_{\nu_i\to\nu_j} = P_{\nu_j\to\nu_i}. \tag{B.3}$$

where $i, j = e, \mu, \tau$.

For $90^\circ \le \xi \le 147^\circ$, the neutrinos only traverse the Earth mantle where $\rho \equiv \rho_m = 5$ g/cm^3 with $Y_e \equiv Y^m_e = 0.49$.

2. For $147^\circ \le \xi \le 180^\circ$

$$\begin{aligned}
P_{\nu_\mu\to\nu_e} &= \sin^2\theta_{23}(1-\alpha^2-\beta^2), \\
P_{\nu_e\to\nu_\tau} &= \cos^2\theta_{23}(1-\alpha^2-\beta^2), \\
P_{\nu_\mu\to\nu_\tau} &= \sin^2\theta_{23}\cos^2\theta_{23}[\alpha^2+\beta^2+1-2(\alpha\cos\delta+\beta\sin\delta)],
\end{aligned} \tag{B.4}$$

where

$$\begin{aligned}
\alpha &= \cos(2\varphi^m)\cos(\varphi^c) - \cos(2\theta^c_{13}-2\theta^m_{13})\sin(2\varphi^m)\sin(\varphi^c), \\
\beta &= -\cos(2\theta^m_{13})[\sin(\varphi^c)\cos(2\varphi^m)\cos(2\theta^c_{13}-2\theta^m_{13}) + \cos(\varphi^c)\sin(2\varphi^m)] \\
&+ \sin(2\theta^m_{13})\sin(\varphi^c)\sin(2\theta^c_{13}-2\theta^m_{13}), \\
\delta &= \frac{(M^m_{13})^2+(m^m_{13})^2}{4E}\times L^m + \frac{(M^c_{13})^2+(m^c_{13})^2}{4E}\times L^c,
\end{aligned} \tag{B.5}$$

with

$$\varphi^{m(c)} \quad = \quad 1.27\frac{\Delta_{31}^{m(c)}}{2E}L^{m(c)}. \tag{B.6}$$

Here $L^{m(c)}$ is in km and E is in GeV. We note that the upper index "m" denotes the parameter of the Earth mantle and "c" denotes the parameter of the Earth core. Hence L^m is the neutrino path-length traversing the Earth mantle and L^c is the neutrino path-length traversing the Earth core. In addition, the Earth core has the constant density $\rho \equiv \rho_c = 12$ g/cm^3 with $Y_e \equiv Y_e^c = 0.467$.

Bibliography

[1] S. W. Barwick, *Astroparticle physics with high energy neutrinos*, lectures presented at 28th SLAC Summer Institute on Particle Physics: Neutrinos from the Lab, the Sun, and the Cosmos (SSI 2000), Stanford, California, USA, 14-25 Aug 2000; H. Athar, arXiv:hep-ph/0209130; H. Athar, arXiv:hep-ph/0212387.

[2] G. Domokos and S. Kovesi-Domokos, arXiv:hep-ph/9801362; arXiv:hep-ph/9805221. See also, D. Fargion, Astrophys. J. **570**, 909 (2002) [arXiv:astro-ph/0002453].

[3] X. Bertou, P. Billoir, O. Deligny, C. Lachaud and A. Letessier-Selvon, Astropart. Phys. **17**, 183 (2002) [arXiv:astro-ph/0104452].

[4] J. L. Feng, P. Fisher, F. Wilczek and T. M. Yu, Phys. Rev. Lett. **88**, 161102 (2002) [arXiv:hep-ph/0105067].

[5] S. Bottai and S. Giurgola, Astropart. Phys. **18**, 539 (2003) [arXiv:astro-ph/0205325].

[6] J. J. Tseng, T. W. Yeh, H. Athar, M. A. Huang, F. F. Lee and G. L. Lin, Phys. Rev. D **68**, 063003 (2003) [arXiv:astro-ph/0305507].

[7] RICE Collaboration, I. Kravchenko *et al.*, astro-ph/0306408; see also, M. Chiba *et al.*, in *Radio Detection of High Energy Particles*, edited by D. Saltzberg and P. Gorham, AIP Conf. Proc. No. 579 (AIP, Melville, NY, 2001), p.204.

[8] http://www.ps.uci.edu/$\sim$ *anita/*

[9] F. F. Lee and G. L. Lin, arXiv:hep-ph/0412383.

[10] L. V. Volkova, G. T. Zatsepin and L. A. Kuzmichev, Sov. J. Nucl. Phys. **29**, 645 (1979) [Yad. Fiz. **29**, 1252 (1979)].

[11] S. I. Dutta, M. H. Reno, I. Sarcevic and D. Seckel, Phys. Rev. D **63**, 094020 (2001) [arXiv:hep-ph/0012350].

[12] B. Rossi, High Energy Particles (Prentice Hall, Englewood Cliffs, NJ, USA, 1952).

[13] A. A. Petrukhin and V. V. Shestakov, Can. J. Phys. **46**, S377 (1968).

[14] R. P. Kokoulin and A. A. Petrukhin in *Proceedings of the XII International Conference on Cosmic Rays* (Hobart, Tasmania, Australia, 1971), Vol. 6.

[15] L. B. Bezrukov and E. V. Bugaev, Sov. J. Nucl. Phys. **33**, 635 (1981) [Yad. Fiz. **33**, 1195 (1981)]. For a recent discussion, see E. V. Bugaev and Y. V. Shlepin, Phys. Rev. D **67**, 034027 (2003) [arXiv:hep-ph/0203096].

[16] P. Lipari and T. Stanev, Phys. Rev. D **44**, 3543 (1991).

[17] J. Pumplin, D. R. Stump, J. Huston, H. L. Lai, P. Nadolsky and W. K. Tung, JHEP **0207**, 012 (2002) [arXiv:hep-ph/0201195].

[18] V. A. Naumov and L. Perrone, Astropart. Phys. **10**, 239 (1999) [arXiv:hep-ph/9804301].

[19] S. L. Glashow, Phys. Rev. **118**, 316 (1960).

[20] For a recent discussion see, H. Athar and G. -L. Lin, Astropart. Phys. **19**, 569 (2003) [arXiv:hep-ph/0108204], and references cited therein.

[21] A. Neronov, D. Semikoz, F. Aharonian and O. Kalashev, Phys. Rev. Lett. **89**, 051101 (2002) [arXiv:astro-ph/0201410]; O. E. Kalashev, V. A. Kuzmin,

D. V. Semikoz and G. Sigl, Phys. Rev. D **66**,063004 (2002) [arXiv:hep-ph/0205050].

[22] E. Waxman and J. N. Bahcall, Phys. Rev. Lett. **78**, 2292 (1997) [arXiv:astro-ph/9701231]; *ibid.,* Phys. Rev. D **59**, 023002 (1999) [arXiv:hep-ph/9807282].

[23] V. S. Berezinsky and G. T. Zatsepin, Phys. Lett. **28B**, 423 (1969). For a recent discussion, see R. Engel, D. Seckel and T. Stanev, Phys. Rev. D **64**, 093010 (2001) [arXiv:astro-ph/0101216].

[24] H. Athar, arXiv:hep-ph/0210244; H. Athar, K. Cheung, G. -L. Lin and J. -J. Tseng, Astropart. Phys. **18**, 581 (2003) [arXiv:hep-ph/0112222].

[25] AMANDA Collaboration, J. Ahrens *et al.*, Phys. Rev. Lett. **90**, 251101 (2003)

[26] N. La Barbera, private communications.

[27] G. W. Hou and M. A. Huang, *Expected performance of a neutrino telescope for seeing AGN/GC behind a mountain*, talk given in 1st NCTS Workshop on Astroparticle Physics, Taiwan, 6-9 Dec 2001, published in its proceedings, pp. 105-116, Eds. H. Athar, G. -L. Lin and K. -W. Ng, World Scientific, Singapore (2002) [arXiv:astro-ph/0204145]. See also http://hep1.phys.ntu.edu.tw/nutel/.

[28] T. Abu-Zayyad *et al.* [HiRes-MIA Collaboration], Astrophys. J. **557**, 686 (2001) [arXiv:astro-ph/0010652].

[29] S. P. Swordy and D. B. Kieda, Astropart. Phys. **13**, 137 (2000) [arXiv:astro-ph/9909381].

[30] Z. Cao, M. A. Huang, P. Sokolsky and Y. Hu, J. Phys. G **31**, 571 (2005) [arXiv:astro-ph/0411677].

[31] For a recent brief review article, see, H. Athar, Chin. J. Phys. **42**, 1 (2004).

[32] Y. Ashie *et al.* [Super-Kamiokande Collaboration], Phys. Rev. Lett. **93**, 101801 (2004) [arXiv:hep-ex/0404034].

[33] Y. Suzuki, in *Proceedings of the 28th International Cosmic Ray Conferences (ICRC 2003), Tsukuba, Japan, 2003*, edited by T. Kajita *et al.* (Universal Academic Press, Inc., Tokyo, Japan, 2004), Vol. 8, p. 75.

[34] T. Kajita and Y. Totsuka, Rev. Mod. Phys. **73**, 85 (2001). For a recent discussion of the forthcoming astrophysical neutrino telescopes, see, A. B. McDonald *et al.*, Rev. Sci. Instrum. **75**, 293 (2004).

[35] H. Athar, Mod. Phys. Lett. A **19**, 1171 (2004).

[36] T. K. Gaisser and M. Honda, Ann. Rev. Nucl. Part. Sci. **52**, 153 (2002).

[37] G. Ingelman and M. Thunman, arXiv:hep-ph/9604286.

[38] T. K. Gaisser, Astropart. Phys. **16**, 285 (2002).

[39] T. Sjöstrand, Comput. Phys. Commun. **82**, 74 (1994).

[40] H. Athar, K. Cheung, G. L. Lin and J. J. Tseng, Astropart. Phys. **18**, 581 (2003).

[41] *Cosmic Rays and Particle Physics*, T. K. Gaisser, Cambridge University Press (1992).

[42] P. Lipari, Astropart. Phys. **1**, 195 (1993).

[43] U. T. Hsu, *master thesis* , NCTU (2005).

[44] M. Thunman, G. Ingelman and P. Gondolo, Astropart. Phys. **5**, 309 (1996) [arXiv:hep-ph/9505417].

[45] V. Agrawal, T. K. Gaisser, P. Lipari and T. Stanev, Phys. Rev. D **53**, 1314 (1996) [arXiv:hep-ph/9509423].

[46] P. Nason, S. Dawson and R. K. Ellis, Nucl. Phys. B **327**, 49 (1989) [Erratum-*ibid.* B **335**, 260 (1990)].

[47] M. L. Mangano, P. Nason and G. Ridolfi, Nucl. Phys. B **373**, 295 (1992).

[48] E. V. Bugaev *et al.*, Nuovo Cimento C **15**, 401 (1992).

[49] B. Rossi, High Energy Particles (Prentice Hall, Englewood Cliffs, NJ, USA, 1952).

[50] S. M. Barr, T. K. Gaisser, P. Lipari and S. Tilav, Phys. Lett. B **214**, 147 (1988).

[51] G. Barr, T. K. Gaisser and T. Stanev, Phys. Rev. D **39**, 3532 (1989).

[52] H. Athar, F. F. Lee and G. L. Lin, Phys. Rev. D **71**, 103008 (2005) [arXiv:hep-ph/0407183].

[53] L. Pasquali and M. H. Reno, Phys. Rev. D **59**, 093003 (1999) [arXiv:hep-ph/9811268].

[54] L. Pasquali, M. H. Reno and I. Sarcevic, Phys. Rev. D **59**, 034020 (1999) [arXiv:hep-ph/9806428].

[55] A. B. Kaidalov and O. I. Piskunova, Z. Phys. C **30**, 145 (1986); L. V. Volkova, W. Fulgione, P. Galeotti and O. Saavedra, Nuovo Cim. C **10**, 465 (1987).

[56] E. V. Bugaev, A. Misaki, V. A. Naumov, T. S. Sinegovskaya, S. I. Sinegovsky and N. Takahashi, Phys. Rev. D **58**, 054001 (1998) [arXiv:hep-ph/9803488].

[57] C. G. S. Costa, Astropart. Phys. **16**, 193 (2001) [arXiv:hep-ph/0010306].

[58] C. G. S. Costa, F. Halzen and C. Salles, Phys. Rev. D **66**, 113002 (2002) [arXiv:hep-ph/0104039].

[59] B. A. Li, Phys. Rev. D **52**, 5165 (1995) [arXiv:hep-ph/9504304].

[60] C. G. S. Costa and C. Salles, arXiv:hep-ph/0105271.

[61] T. K. Gaisser and T. Stanev, Phys. Rev. D **57**, 1977 (1998) [arXiv:astro-ph/9708146].

[62] T. Stanev, Phys. Rev. Lett. **83**, 5427 (1999) [arXiv:astro-ph/9907018].

[63] D. Elsaesser and K. Mannheim, Astropart. Phys. **22**, 65 (2004) [arXiv:astro-ph/0405347].

[64] F. D. Stacey, *Physics of the Earth, 2nd edition* , John Wiley and Sons, London, New York, 1977.

[65] H. Athar, K. Cheung, G. L. Lin and J. J. Tseng, Eur. Phys. J. C **33**, S959 (2004) [arXiv:astro-ph/0311586].

[66] See, for instance, H. Pessard [OPERA Collaboration], arXiv:hep-ex/0504033, and references cited therein.